Synchrotron X-ray Tomography Study of Bone-implant Integration

Ornella Lohéac

Lund, August 2021

LUND UNIVERSITY

VRIJE UNIVERSITEIT BRUSSEL

GHENT UNIVERSITY

Master's Thesis in Biomedical Engineering

Department of Biomedical Engineering
Faculty of Engineering LTH
Lund University

Supervisors: Prof. Hanna Isaksson, Ph.D.
Elin Törnquist, M.Sc.
Joeri Kok, M.Sc.

Examiners: Dr. Maria Pierantoni, Ph.D.
(Lund University)
Prof. Jef Vandemeulebroucke, Ph.D.
(Vrije Universiteit Brussel)

Abstract

Implant loosening is a recurring problem in the field of orthopedics, typically resulting in a physical and financial burden for the patient. Proper integration of orthopedic implants within host bones is a fundamental requirement for the successful function and limited risk of failure of implants which, in-vivo, must support various loading conditions. This implant fixation is highly dependent on the amount and quality of the bone formed around the implant post-surgery.

Previous studies have used mechanical loading, combined with lab or medical source X-ray imaging at macro- and micro-scale, as well as digital volume correlation (DVC), to successfully characterize the structural and mechanical properties of the bone-implant interface of small animals ex-vivo. Nevertheless, these studies had limitations due to imaging artifacts, low image resolution and small sample sizes.

In this study, both the number of specimens and the image resolution were increased compared to previous studies. Here, 21 rat tibiae were implanted with polyether ether ketone (PEEK) implants and imaged at high resolution using X-ray synchrotron micro-Computed Tomography (μCT) during *in situ* pull-out of the implants. The PEEK implants were filled with a Calcium sulfate-hydroxyapatite (CaS/HA) based bone cement or with a combination of CaS/HA and bioactive molecules (zoledronic acid (ZA) and recombinant human bone morphogenic protein-2 (rhBMP-2)) known to promote bone formation. The experiments were conducted prior to the start of this degree project. The focus of this degree project lay on processing and analyzing the collected data. The quality of the bone-implant interface was quantitatively assessed based on the mechanical properties obtained from the pull-out experiment. Quantitative evaluation was achieved by using the CT data to visualize and quantify the bone formation around the implants. A qualitative assessment of the interface was also performed, analyzing the internal strain distribution through DVC analysis of μCT images. Additionally, the use of DVC as a tool to identify cracks and deformations in the peri-implant bone, in loadsteps prior to failure, was investigated.

Combining PEEK implants with bioactive molecules improved the overall mechanical resistance of the bone-implant interface. Bone volume fraction increased significantly by 250.4%. Furthermore, DVC served as useful tool in visualizing the strain distributions in bone specimens under load-

ing, successfully indicating local regions of deformation and fracturing within the loaded samples, prior to complete failure. Both untreated and treated samples showed comparable modes of failure; the bone failing at the threads and the thin trabecular bone surrounding the implant.

Improving newly formed peri-implant bone quality and quantity could lead to an increased quality of life for patients and a decrease of the financial burden caused by orthopedic surgery.

Key words **- Bone-implant, Digital volume correlation, Micro-computed tomography, PEEK, Synchrotron**

Preface

As a Biomedical Engineering Master's student at the Vrije Universiteit Brussel joint Ghent University (Belgium), I had the possibility to carry out part of my academic career abroad, under the Erasmus+ program. This led to the incredible experience of conducting my Masters' Thesis as an exchange student at Lund University. Due to the global Covid-19 pandemic and the travel restrictions following from this, my exchange and therefore also this Master's thesis were conducted remotely from Belgium. Nevertheless, this has been a unique and enriching learning experience for which I am extremely thankful.

This Master's degree project was carried out during the spring semester of 2021, within the Biomechanics research group, at the Department of Biomedical Engineering, Lund University. This Master's dissertation is submitted to obtain the academic degree of Master of Science in Biomedical Engineering.

Acknowledgments

First and foremost, I would like to express my immense gratitude to my supervisors, Prof. Hanna Isaksson, Ph.D. student Elin Törnquist and Ph.D. student Joeri Kok for their excellent guidance through the multitude of challenges to be expected in the conduct of a degree project. Thank you for your patience and constant availability, the amazing communication, the brainstorming sessions, and for continuously wanting to share your knowledge with me. I could no have hoped for better mentors to help me with this final academic project.

Thank you to everyone in the Biomechanics group. Even though we could not meet in person before July, you made me feel included from the first online meeting and made the 797 km distance separating Brussels from Lund seem a little shorter.

To my family, thank you for providing me with unconditional love and support through the process of writing this degree project.

Finally, to my exceptional friends, I cannot thank you enough for the countless late night pep talks, continuous encouragements, and memorable breaks. You have been my greatest source of motivation.

This accomplishment would not have been possible without any of you.

Contents

List of Abbreviations

μCT micro-computed tomography

2D two-dimensional

3D three-dimensional

BMP-7 bone morphogenic protein - 7

BV bone volume

BV/TV bone volume over total volume

CaS/HA calcium sulfate-hydroxyapatite

CT computed tomography

CW correlation window

DVC digital volume correlation

FFC flat field correction

FOV field of view

NS node spacing

PEEK polyether ether ketone

rhBMP-2 recombinant human bone morphogenic protein - 2

ROI region of interest

SW search window

ZA zoledronic acid

1 Introduction

Orthopedic implants are used when there is a need for stabilizing fractured bones or for replacing bones and joints. Bone and joint replacements are generally necessary for patients suffering from accidents and joint diseases [1, 2]. These implants will need to function under various conditions *in vivo*, thereby making proper integration into the host bone a fundamental requirement [2]. In the Swedish Hip Arthroplasty Register Annual report of 2019, it was mentioned that between 2010 and 2019, implant loosening was the main cause for surgical revision [3]. Unfortunately, this problem is not only limited to hip arthroplasty; implant loosening is a commonly arising problem in the field of orthopedic surgeries [4, 5]. Additionally, reoperations are known to cause a substantial increase in cost [3, 6].

The long-term stability of implants relies on adequate bone-implant integration, which depends on the quality and quantity of the newly formed bone around the implant. Studies have evaluated the effect of treating implants to improve this implant stability [6, 7, 8]. The treatments used to that end consisted of various combinations of bioactive molecules, such as bone morphogenic protein - 7 (BMP-7), zoledronic acid (ZA), and recombinant human bone morphogenic protein - 2 (rhBMP-2), which are already used clinically. These molecules are known to stimulate the production of bone [6, 7]. The molecules in these previous studies were administered in the form of a putty, or slowly released from the implant with the use of a carrier, typically a calcium sulfate-hydroxyapatite (CaS/HA) based bone cement. Slow release of bioactive molecules has shown to cause increased bone formation.

Assessing orthopedic implant stability has been the focus of multiple studies (e.g., [6, 7, 8, 9, 10]), where the quality of the bone-implant integration was assessed through the structural and mechanical properties of the bone-implant interface with the use of mechanical testing and tomographic imaging. The main mechanical properties of the bone that were investigated with pull-out tests were: the peak force, the stiffness, and the absorbed energy of the bone. One of the structural properties most relevant for bone implant integration is bone volume over total volume (BV/TV). The data collected in these studies indicated a clear improvement in osseointegration, newly formed bone volume and mechanical properties of the peri-implant bone for the treated implants. The studies demonstrated that the BMP molecules stimulated regeneration of bone and enhanced

bone formation, while the use of ZA reduced the bone resorption effect [6, 7].

Traditionally, metal alloys are used as a base material for the implants [7, 8, 9, 10]. However, these implants are known to cause imaging artifacts during X-ray based imaging, hindering the correct quantification of bone ingrowth [6]. To overcome the limitation of imaging artifacts, polyether ether ketone (PEEK) implants can be used. Additionally, previous studies employed laboratory source X-ray imaging and were based on a limited number of specimens (N = 2), limiting the imaging resolution and accountability for biological variation, respectively. Synchrotron source imaging can be chosen as imaging modality to further improve image quality and enable a more detailed analysis of the newly formed bone around the implants.

At Lund University, a new project was launched within the Biomechanics group where 21 PEEK implants were placed in rat tibiae. With this present study, the micro-structure of newly formed bone around treated (Trtd, n = 11) and untreated (Ctrl, n = 10) implants is investigated, using high resolution synchrotron μCT and more specimens than before (N = 21). The bioactive molecules used to treat the implants are ZA and rhBMP-2, and the carrier of these molecules is a CaS/HA based bone cement. This study design enables a more detailed analysis of the newly formed bone and better accountability for biological variation within the specimens. This framework forms the basis for the work in this Master's thesis.

2 Aims

The aim of the thesis project is to assess the quality of the bone-implant integration of drug treated PEEK implants compared to a control group with no drugs. This is done qualitatively, by investigating the mechanical properties of the bone-implant interface from a pull-out experiment, and computing internal strain distributions obtained from digital volume correlation (DVC) analysis of micro-computed tomography (μCT) obtained concurrently with the mechanical testing. Moreover, a quantitative bone volume (BV) analysis from the X-ray μCT data is performed, which quantifies the amount of new bone formed around the implant by comparing the newly formed bone volume with the total volume of a certain volume extending 0.8 mm from the implant surface, i.e., the bone volume/total volume (BV/TV).

The following research questions will hereby be answered:

- What are the effects of the treatment on bone ingrowth volume?
- What are the effects of the treatment on mechanical properties of the newly formed bone?
- What are the effects of the treatment on strain distribution, and failure mode of the newly formed peri-implant bone?
- Can Digital Volume Correlation help identify deformations in the peri-implant bone before failure?

A significant improvement in the bone-implant integration quality and bone ingrowth volume of the specimen from the drug treated group is expected, as well as enhanced mechanical characteristics of the newly formed bone interface.

The results from this research will lead to a deeper understanding of how and to what extent drug treatments can influence the quality of bone-implant integration. It will serve as a solid base for possible extrapolation of the results to human orthopedic applications and further studies about alternative drug treatments and imaging for implants.

3 Background

In this section, the theory behind the methods is presented. Bone structure and healing properties, along with an overview of implant stability, is presented. The working principle of computed tomography (CT) is explained, and the applications used in this thesis are presented. The chapter ends with a review of previous work on the characterization of bone-implant interface quality.

3.1 Bone

3.1.1 Composition and Structure

Bone is a dynamic, living tissue that is continually evolving to adapt to the externally applied biomechanical loads [11, 12]. The mechanism of adapting the structure to applied forces is known as modeling and remodeling. Remodeling also includes repairing the bone tissue by removing microdamage in the tissue and replacing it with new and mechanically stronger bone [12]. The first bone to be formed is immature (woven) bone, which is quickly replaced by stronger, more mineralized, mature bone [13].

Cortical bone and trabecular bone are two morphological types of mature bone present in e.g., long bones such as the femur or tibia [13] (Figure 3.1(a)). The dense and solid cortical bone provides protection, support and resistance to applied stresses. It is mainly found surrounding the medullary cavity, forming the wall of the diaphysis. Epiphyses are the extended bone structures at the extremities of long bones, which consist primarily of trabecular bone that provides them with support and allows for storage of bone marrow. Together, cortical, and trabecular bone aid with supporting the body's locomotion [14].

Different bones have different ratios of cortical to trabecular bone, depending on the bending moments and stresses they are subjected to [12, 15]. Cortical bone is more present in bone areas where the applied stresses come from a limited amount of directions, while trabecular bone is predominantly present in areas where low stresses are applied or the stresses originate from multiple directions (Figure 3.1(b)) [14].

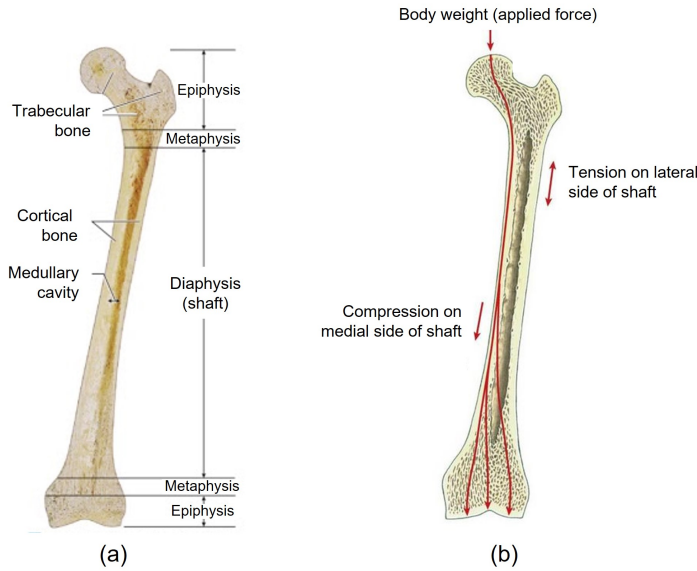

Figure 3.1: Bone Structure. (a) Structure of a representative long bone (the femur) in longitudinal section. (b) The distribution of forces on a representative long bone, illustrating the functional relationship between compact and spongy bone. [Adapted after [14]]

3.1.2 Fracture Healing

A bone fractures when it experiences a strain exceeding its upper limit of bone strain [16]. Luckily, after fracture or injury, bone can repair itself to a certain extent. The degree of repair depends on one's age and medical condition; fracture healing is significantly reduced with aging [17]. Through a set of subsequent cycles of bone formation and bone resorption, injured bones undergo remodeling which allows for the restoration of their pre-fracture mechanical properties with minimal scarring [14, 16, 18].

Healing of a bone fracture occurs under two forms: direct and indirect healing. Direct healing, commonly called primary healing, only occurs under stable conditions when the fragments of the fractured bone are in direct contact, usually on account of compression, proper positioning and alignment of the bone fragments, which are achieved by performing a surgical procedure [19, 20]. The bony ends of the fragments are thereby joined and healed without the formation of a callus, i.e., a mass of bony healing tissue which forms a bridge at the ends of broken bone, allowing for complete reconstruction of the bone and consequently, for the bone to recover to a form close to its original form [19, 20, 21].

Indirect healing usually occurs where some motion occurs at the fracture site, e.g., external fixation or internal fixation of comminuted fractures [19]. A callus will ensue from this healing process [22]. As surgical interventions are not required in most bone fracture cases, bone fractures will generally heal by indirect healing rather than by direct healing [19].

The healing of bone is a complex physiological process composed of 3 main phases; the inflammation, repair, and remodeling phase (Figure 3.2) [17, 22]. It is important to note that these 3 phases overlap temporally when transitioning from one phase to the next.

When a bone fractures, the blood vessels inside the bone are ruptured, causing the fracture region to fill with blood. Instantly, the initial phase of the healing cascade is activated. In this first phase, referred to as the inflammation phase, a hematoma is formed. Together, cells, growth factors and cytokines clear the fracture site of any debris and necrotic tissues [17, 23, 24]. It takes approximately 24 hours for the inflammatory response to peak and this phase will last for about 5 to 7 days [17, 19, 25].

Once the hematoma has fully coagulated and the fracture site has been cleared, the repair phase can begin (Figure 3.2) [19]. It is in this phase that direct and indirect healing differ. In indirect healing, the reparative phase consists of the forming of a soft callus of cartilage that will be replaced by a hard callus of bone that will provide rigidity and mechanical stability to the fracture site [17, 26]. The soft callus formation bridges the gap between bone fragments at the fracture site. By means of intramembranous or endochondral ossification, the soft callus is replaced by a hard callus. In direct healing, the callus formation is bypassed, and the connected bone fragments are healed directly by osteoclasts and osteoblasts activities [22].

Both direct and indirect healing cascades are finalized with the remodeling phase in which the fast less organized woven bone is removed, and new well-structured lamellar bone is created [17, 27]. Once the bone fragments have bonded, the pre-fracture anatomy and physiology of the bone is restored. This process takes years to complete depending on factors such as the fracture location, fracture type and the patient's medical condition [17].

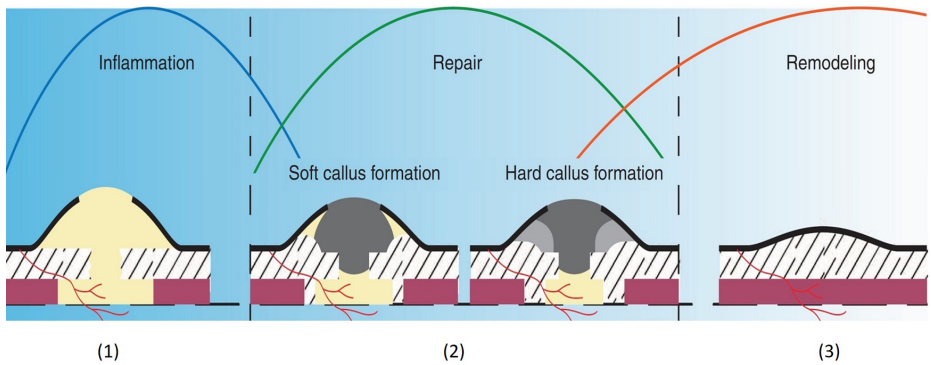

Figure 3.2: Overview of the three phases of healing during indirect healing of bone where yellow represents vascularized tissue; dark gray, fibrous (scar) tissue; light gray, cartilaginous tissue and dashed regions represent the bone. (1) Inflammation phase. (2) Repair phase containing the soft and hard callus formation. (3) Remodeling phase. [Adapted after [22]]

3.1.3 Fracture Healing with an Implant

In the cases where bone is not able to heal correctly, orthopedic implants are used. A surgical intervention is also typically needed for fractures that need realignment or fixation to heal correctly. It is crucial that the implants used do not cause further bone fractures or inhibit the previously discussed cascades of bone healing [17]. Factors that need to be considered when choosing the implant are surface, mechanical, and chemical properties, as well as material biocompatibility. Careful consideration must also be given to the method of surgical implantation. The goal of the healing process is to create a bone-implant bond that enables to bear the biomechanical properties of uninjured, healthy bone [27].

When it comes to the early failure of implants, failure to establish proper osseointegration is one of the major causes [28]. Osseointegration can be considered a measure for implant stability and is successful when an implant and the bone in which it has been implanted are in contact, enabling no relative movement of the implant even under functional loading [29, 30].

Long-term stability of an implant is thus dependent on the quality and quantity of bone integration and strongly correlates to its primary and secondary bone fixation [30, 31]. Primary fixation is obtained by means of a tight press-fit of the implant into the bone, and secondary fixation depends on the biological anchoring in bone [32]. Primary fixation must be obtained directly after the implant surgery. Once fixation is achieved,

the process of long-term or secondary fixation can be initiated. The faster the secondary fixation will be completed, the better the overall fixation quality or osseointegration of the implant [31]. Primary bone fixation can be augmented by using bone cement, while secondary fixation is improved using drugs [31]. Bone cements are materials that form a paste after mixing of a powder and liquid phase. Once implanted in the body, the paste will set and ensure bone-material contact in the defect [33]. The bone cement used in this project is a calcium sulfate-hydroxyapatite (CaS/HA) based cement, CERAMENT®, designed to resorb at the same rate that bone forms. Its injectable, moldable and drillable properties make it a good bone void filler for implant fixation in orthopedic surgeries [34].

When an implant is brought into its host bone through surgical intervention, blood will flow from the bone, making it the first substance the implant encounters. This blood accumulation around the foreign material will cause a hematoma to form around the implant, like a fracture hematoma [27]. The processes following resembles the steps previously described for fracture healing. The final mechanical integrity of the bone-implant interface is obtained from the remodeling phase and is dependent of the degree of remodeling and the bone-implant stability [35].

Several techniques can be used to promote bone formation and speed up the process of obtaining secondary bone-implant stability. This includes manipulating the implant's surface topology to chemical and/or biomolecular alterations of the implant's surface and/or contents. When using surface coatings, the surface of the implant can be covered with bioactive molecules known to stimulate bone formation (e.g., hydroxyapatite (HA), ZA or rhBMP-2) [6, 29]. These surface coatings are meant to mimic biochemical and nanostructure properties of human bone [30]. Multiple studies report improved bone properties of the peri-implant bone when using drug coated implants instead of uncoated implants [36, 37, 38]. Moreover, recent studies have analyzed the effect of placing the bioactive molecules directly in the cement inside the implant, releasing the drugs slowly and affecting the bone locally by doing so [6].

3.2 Mechanical Properties of the Bone-Implant Interface

A common way of assessing implant stability is by performing pull-out tests to quantify the mechanical properties of the peri-implant bone [9]. During such a test, the implant is attached to a device that measures the force and displacement during continuous or incremental pull-out. From

the recorded data, parameters such as maximum force and displacement at failure, stiffness, and fracture (absorbed) energy of the interface can be obtained (Figure 3.3). These parameters serve as a useful tool for the analysis of fracture [9, 39, 40].

Peak Force is the highest force supported by the sample before failure. A too low value will mean the bone-implant interface cannot withstand much force and will more quickly lead to revision surgery and pain [10, 41]. [N]

Peak Displacement is the displacement corresponding to the maximum force [10]. [mm]

Stiffness is defined by the slope of the linear part of a force-displacement curve ($\frac{\Delta F}{\Delta l}$). It thus expresses the resistance of the screw fixation to elastic deformation. A high stiffness value is found for brittle bone and a low value is typical for ductile bone. If the bone at the interface is too stiff, it will require less energy to fracture [8, 40, 41]. [N/mm]

Fracture energy is calculated as the area under the loading curve until the point of peak force [10]. This represents the amount of energy that can be absorbed by the sample before failure. If the energy transferred into the bone, through trauma, exceeds this value of absorbable energy, the bone at the interface will break [42]. [N/mm = J/mm^2]

Another aspect that characterizes the mechanical properties of bone is the strain (ϵ) experienced under loading. Assessing the internal strains in bones can give valuable clinical information about the mechanisms of fracture and crack initiations [43]. Strain is defined as the ratio of a sample's geometrical deformation along the axis of response to an applied load (l) and the original unloaded sample length (l_0) (Equation 3.1) [44].

$$\epsilon = \frac{l - l_0}{l_0} \quad [dimensionless] \tag{3.1}$$

The strain of 3D solid materials is defined by 6 components: 3 normal or volumetric strain components ($\epsilon_x, \epsilon_y, \epsilon_z$), and 3 shear strain components ($\gamma_{yz}, \gamma_{xz}, \gamma_{xy}$) [46] (Figure 3.4).

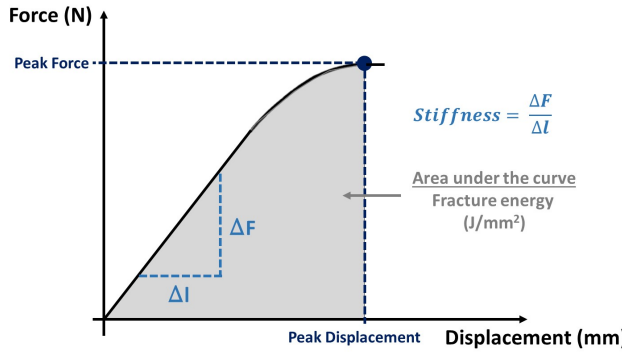

Figure 3.3: Force-displacement curve with the conceptual overview of maximum force and displacement at failure, stiffness, and fracture energy. [Redrawn from [45]]

Normal strains are defined as the changes in length of the material along a specific direction (X,Y or Z-direction) [46].

Shear strains occur when sideways forces are exerted on the material, which cause an angular change in points of the material. The strains are defined by these changes in angles with respect to two different directions (X and Z, Y and Z, X and Y-directions) [46].

The normal and shear strain at a point in the material can be related to its displacement by defining the strain as the variation of the rate of displacement and angle per unit length [46].

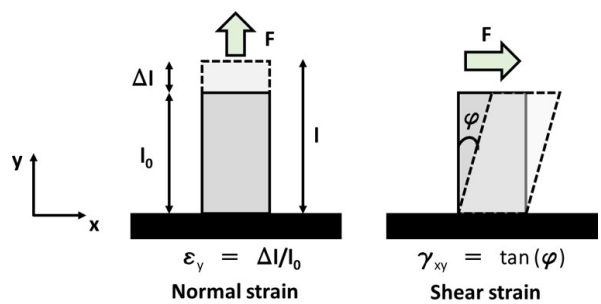

Figure 3.4: Conceptual overview of normal (ϵ) and shear (γ) strain in a 2D plane. Generally, strain occurring in a material is a combination of both these types of strain. [Redrawn from [45]]

3.3 Imaging of Bone

The process of imaging a three-dimensional (3D) object and representing it as a volume based on multiple two-dimensional (2D) images is commonly referred to as tomography [47, 48]. Computed Tomography (CT) is the most widely used tomographic modality in radiology departments [49].

3.3.1 Working Principle of Computed Tomography

Computed tomography is an imaging technique based on the principle of transmission of X-rays. In essence, X-rays are produced from a source directed to an object and are measured by a detector [50]. With computer processing, X-ray images taken from different angles are combined and reconstructed into a 3D image [51].

X-rays will penetrate through the imaged object, losing some intensity in the process due to absorption and deflection or scattering by the tissues inside the body [51]. The amount of absorption and deflection depends on the composition and density of the material, as well as the energy of the X-rays; increasing density, and decreasing energy and atomic number will result in increased absorption [52].

Most commonly, X-ray images are based on the attenuation of the energy of incident X-rays (Figure 3.5A). Since the attenuation is dependent on material composition, there will be contrast between different materials within an object in the tomographic images [50]. The visualization of this variation on X-ray attenuation is referred to as absorption-contrast imaging [53]. Some areas of the images will be radiopaque. These areas correspond to materials in the object that block the passage of X-rays to a certain extent and result in a light gray or white appearance on the film of the photographic plate. Areas that are less radiopaque, e.g., air, will be imaged as darker shades of gray or black [51].

If the imaged object contains materials with low or similar absorption properties, phase-contrast imaging can instead be used to visualize the internal structures (Figure 3.5B). This imaging method monitors the phase shifts of X-rays travelling through the object and is often used for imaging objects composed of lighter elements [54]. By passing through the object, the incident X-ray wavefront will change in shape before propagating over a certain distance until it reaches the detector [55].

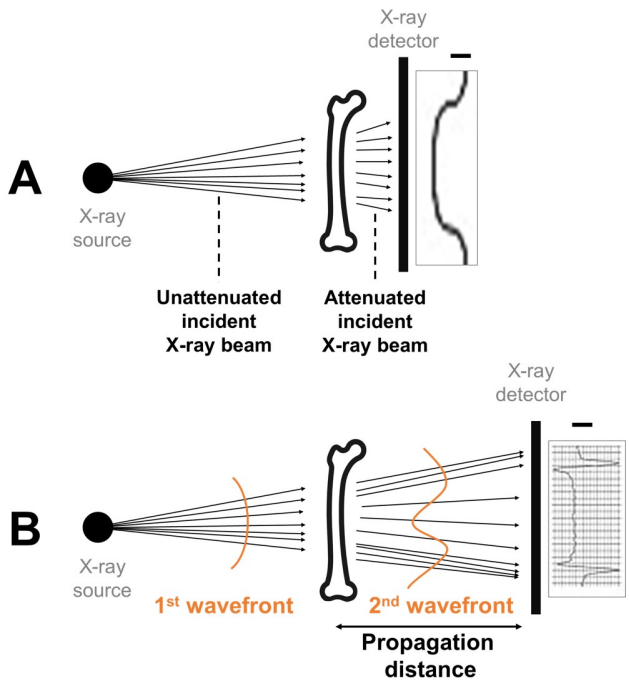

Figure 3.5: Comparison of absorption- and phase-contrast X-ray imaging methodology. Parameter I expresses the intensity measured by the detector. (A) Absorption-contrast imaging. (B) Phase-contrast imaging. [Redrawn from [55]]

3.3.2 X-ray Sources and Applications

X-rays can be produced by various sources, such as X-ray tubes and synchrotrons [7, 50]. Deciding what source to use depends on the field and type of application for which the X-rays are needed.

Medical X-ray sources are used for medical applications where the source and detector rotate around a sample to acquire 3D image volumes under different angles [56]. CT was the first modality to be introduced in clinical radiology in 1973 to image the anatomy of the human body [51]. Its non-invasive property and spatial resolution of 1-2 mm for meter-scale to decimeter-scale objects make it a useful diagnostic tool in medical imaging [48, 57, 58]. As bone is radiopaque, CT is a good modality to focus on this specific body tissue, offering good contrast of bone to soft tissue. Bone will appear as white on the tomographic images [51]. Since 1973, CT has become the gold standard for the evaluation of the degree of osseointegration, mainly due to its non-invasiveness [59, 60, 61].

CT that is not used for direct clinical needs is called industrial or laboratory CT. Laboratory X-ray sources are mainly used for scientific research in various fields such as biological sciences, geosciences, material sciences and even food sciences [62, 53]. The structures studied with laboratory CT are smaller than the ones in medical imaging, enabling higher resolution, i.e., at μm resolution. The modality used to obtain such resolution is known as micro-computed tomography (μCT). The fundamentals of μCT, are identical to the previously discussed X-ray CT imaging; μCT scanners capture a series of 2D planar X-ray images and reconstruct the data into 2D cross-sectional slices which can be further processed into 3D image volumes. Contrary to medical CT scanners, the X-ray source and detector do not rotate around the sample during μCT imaging, it is the sample itself that is rotated while the source and detector stay static [56]. The X-ray source used in μCT systems can produce X-rays ranging from 20 to 100 keV, producing high-resolution 3D image data. The resolution of μCT can be tailored by changing the distances between source, sample, and detector [63].

The major advantage obtained from using μCT is that morphological features such as porosity, bone thickness, volume fraction, density, particle size, voids, and fiber orientation can be studied with great spatial resolution using this imaging tomography [64].

In laboratory and medical sources, X-rays are produced by accelerating electrons ejected from a heated cathode filament towards a solid metal object, the anode. When the electrons strike the surface of the anode, X-rays are generated and evacuated to be passed through the object being imaged [50, 49] (Figure 3.6). Different applications require different X-ray energy and wavelength ranges (Figure 3.7).

Nevertheless, the quality of images achievable by using medical and laboratory source X-ray CT or μCT is limited [65]. A way to increase the quality, and thus the amount of detail visible in the material under study, is by using synchrotron generated X-rays [66].

Synchrotrons are extremely powerful electron accelerators, creating high energy X-rays that are mainly used for the structural analysis of matter [66]. The electrons are firstly generated within an electron gun that runs high voltage electricity through a tungsten-oxide disk which serves as cathode. The electrons leaving the cathode are accelerated to a speed close to the speed of light ($3 \cdot 10^8 \frac{m}{s}$) and pulled towards a linear accelera-

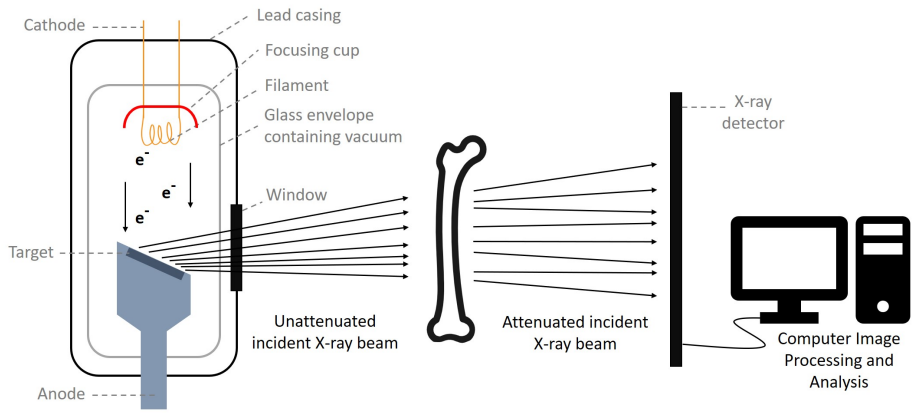

Figure 3.6: Diagram showing the generation of X-rays in a Roentgen tube (Left) and an overview of the simplified process of X-ray imaging. [Redrawn from [67] and [52]]

tor who will bring them to a booster ring before traveling to the storage rings [66]. The storage rings of the synchrotron are composed of multiple straight sections creating a circular-like shape. To make the electrons change directions and follow the circular-like path, dipole magnets are used, causing the production of photons. Each storage ring is surrounded by beamlines, where emitted X-rays go to be directed towards specific experimental workstations where they will be used for research purposes [68]. The emitted beams can be filtered inside the beamlines in order to keep only one wavelength, making synchrotron radiation monochromatic [66]. One such synchrotron radiation facility is the MAX IV, which is located in Lund.

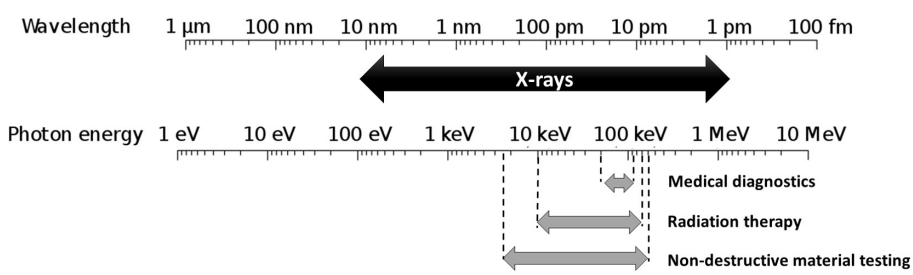

Figure 3.7: Overview of X-ray wavelengths and photon energies for various applications. Acceleration voltages can vary between 10 and 500 keV depending on the application; 90-140 keV for medical diagnostics, 10-300 keV for radiation therapy and up to 500 keV for material testing [49]. [Redrawn from [69]]

Synchrotron-generated X-ray beams allow for an improved brilliance, spatial resolution (below 1 μm) and contrast [65]. The term brilliance refers to the brightness per mm^2 and is therefore maximized when the X-ray beam size is as small as possible and the photon flux is as large as possible. The brilliance of synchrotrons is typically a billion times higher than laboratory sources, allowing for the study of small structures (μm- to nm-scale) and a deeper penetration of the studied material, resulting in more detailed imaging [68]. Furthermore, synchrotron radiation can be of great use in biomedical applications such as the imaging of bone-implant interfaces as it has a fast image acquisition while providing high quality images [8]. The drawback of this radiation source is the resulting high radiation doses which may affect mechanical properties of the imaged material [8]. Studies have reported that bone characteristics, such as strength, ductility, and fracture energy of healthy bone specimens are severely reduced when using an irradiation dose higher than 35 kGy [7, 70].

3.3.3 CT Imaging Artifacts

Besides the radiation doses caused by X-ray imaging and the cost of such tomography, another noteworthy limitation of CT imaging is the appearance of image artifacts. Image artifacts can originate from different sources: physics-based artifacts, patient-based artifacts, scanner-based artifacts, and helical and multi-sectional artifacts [71]. Physics-based artifacts are related to physical processes occurring during the CT data acquisition while helical and multi-sectional artifacts are caused by the process of image reconstruction [71].

Beam hardening is the main physics-based artifact, causing the appearance of dark bands or streaks between dense objects on the CT images. The faster absorption of lower-energy photons of a photon beam traveling through material make the beam "harder" and are the cause of this artifact [71]. By imaging with a monochromatic X-ray beam using a synchrotron source, this artifact is reduced as all photons have the same energy [65].

Ring artifacts (Figure 3.8A) are a common type of scanner-based artifacts. They are caused by the miscalibration or failure of one or more pixels in the detector. The name refers to the observation of full or partial circles centered on the rotational axis when these artifacts occur [63].

Metal artifacts (Figure 3.8B) occur when metallic objects are present in the scanned field, making them patient-based artifacts. Incomplete attenuation profiles are obtained because of metal artifacts. Special software corrections, such as interpolation techniques, can be used to minimize the effect of these artifacts on the final attenuation profiles [71].

Fixed pattern noise (FPN) is recognizable by the systematic pattern of brighter and darker pixels in different images taken under the same imaging conditions [72]. FPN can be caused by X-ray beam inhomogeneity, a non-uniform sensitivity of the pixels of the detector, dark currents in the detector or scratches and/or dust accumulated by the X-ray detector screen [73]. Dark currents refer to small electric currents that are generated in the detector, even when no radiation is entering the detector [74].

The conventional correction for this artifact, flat field correction (FFC), employs flat fields (f) and dark fields (d) to normalize the acquired projections (p_i), thereby removing the FPN. A flat field is a projection image acquired without the sample, with the X-ray source being turned on. This will correct for X-ray beam inhomogeneities and non-uniform detector response. A dark field is a projection obtained without the presence of a sample, and without X-ray illumination, which corrects the effects caused by dark currents [73].

As artifacts can degrade the quality of CT images, it is important that these artifacts are corrected before any analysis of the samples are carried out; either during initial image reconstruction or later, during post-processing [63, 71].

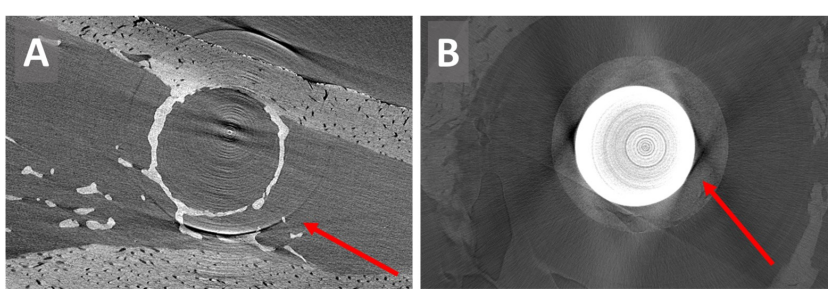

Figure 3.8: X-ray artifacts. (A) Synchrotron based X-ray tomography image showing ring artifacts. (B) Micro-CT scan with a metal artifact due to a nickel (Ni) bead.

3.4 Digital Volume Correlation

A non-invasive experimental technique used to quantify 3D strains is Digital Volume Correlation (DVC) [43]. DVC refers to tracking translations of small sub-volumes between two subsequent 3D images [10, 75]. If the imaged object is being loaded during image acquisition, internal deformation can be tracked using DVC. The general working principle of DVC can be described as defining a sub-volume within the "reference" image volume of the unloaded or smallest loading step (Figure 3.9A), and then finding its best match within the "deformed" image volume of the subsequent loading step (Figure 3.9B). The matching is performed based on the similarity of the sub-volumes' grayvalue patterns. DVC outputs measured internal displacements for multiple sub-volumes, based on which tensor strain fields of a sample subjected to experimental loading can be computed [9, 76]. As deformities are recognizable by their high strain values, with the use of DVC and the full-field strain measurements it makes, tracking of the evolution of internal strain fields leading up to a crack or other large failure is made possible, and insight on the heterogeneous mechanical responses of materials can be gained [76].

For DVC, the estimated maximum displacements between different loadsteps are required to fall within a set range of pixels around the analysis points or nodes, defined by the search window (SW). Additionally, the size of the region to be tracked, i.e. correlation window (CW), and the spacing between nodes, the node spacing (NS), also need to be defined [76, 77] (Figure 3.9A). The estimates for the correlation window and search window can be obtained by visual identification of the displacements when comparing the reference and deformed image volumes manually [76]. Running a DVC analysis with a high number of nodes, i.e., small node spacing, covering the whole range of displacements in 3D, is computationally expensive. Hence, it is recommended to be as precise as possible when defining the input parameters.

The first step of the DVC process will define a subset of pixels surrounding each node (CW) [76]. Next, for each node within the SW, the subset of pixels in the deformed image best matching its subset in the reference image will be identified. The similarity of the subsets of pixels is typically based on the statistical measure of normalized correlation coefficients. A typical scale goes from 0-100%, with 100% expressing a perfect correlation or match between the reference image subset and the deformed image subset. The best matching subset found in the deformed image, defines

the 3D displacements, i.e., integer numbers of pixels in every direction (Figure 3.9B-C). It is possible to obtain a more realistic displacement by performing a sub-pixel refinement. To that end, different procedures can be performed [76, 78]. The two methods used in this project are the correlation coefficient (CC)-interpolation and the image-interpolation. The CC-interpolation procedure uses correlation functions to compute the similarity between sub-volumes. It will interpolate a set of correlation coefficients corresponding to integer displacements by a mathematical function. The maximum of this function gives the sub-pixel resolution displacement. With image interpolation, a subset of the deformed image is displaced until a match is found with the reference image, thereby making it more computationally expensive. Finally, the 3D strain fields can be computed based on the 3D displacements (Figure 3.9D).

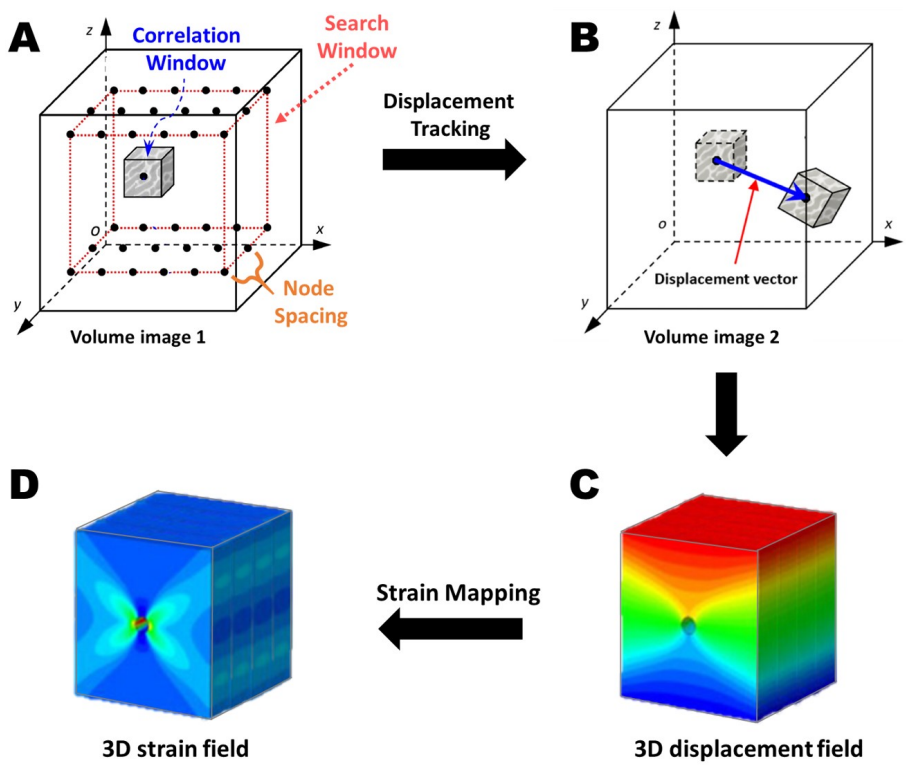

Figure 3.9: Schematic of the DVC procedure (A-D). (A) Definition of the CW, SW and NS in the reference image volume. (B) Displacement tracking by comparison with the deformed image volume. (C) Overview of the displacements. (D) Calculation of the strains based on the displacement fields. [Adapted from [79, 75]]

The accuracy and precision of the resulting displacement and internal strain fields can be assessed by performing a DVC analysis on a virtually translated image volume of one sample. By applying 3D displacements of a few known pixels to the image volume, the accuracy and precision of the displacement fields can be defined. The expected 3D displacements are namely the number of pixels by which the second image volume was translated, and the strain should be zero in all nodes. From the fields that were obtained from the DVC analysis, the mean (accuracy) and standard deviation (precision) of every displacement (in X, Y and Z-direction) and the strain components (i.e., the 3 normal strain and 3 shear strain components), can be calculated [8].

3.5 Previous Studies Assessing Implant Stability

Multiple studies analyzing implant stability and bone-implant integration have been conducted by the Biomechanics group at Lund University, e.g., [6, 7, 9, 10].

A first study was done by *Le Cann et al.* [9] in 2017 to characterize the bone-metal implant interface in the proximal tibia of two male Sprague Dawley rats using DVC of *in situ* loading, imaged with neutron tomography. The stability of implants was assessed by evaluating the ex-vivo mechanical resistance of the newly formed bone surrounding the untreated steel implants and BMP-7 treated titanium implants. The authors used neutron tomography instead of X-ray tomography to sequentially image the pull-out tests as X-ray tomography is known to cause artifacts when imaging metallic objects (See Section 3.3.3). The images acquired had a pixel size of 27 μm. The focus of this study mainly lay on identifying if neutron tomography could be considered as a potential alternative for characterizing the mechanical response of bone-implant interfaces of metallic implants. Indeed, this imaging modality allowed for the identification of cracks and deformations of the bone during mechanical loading, and a good quantification of bone ingrowth around the unloaded implant [9]. The main limitation of this study is the limited number of specimens analyzed (N = 2), due to the long imaging times, and the low resolution of the imaging technique.

In 2019, *Le Cann et al.* [7] investigated the mechanical characteristics of bone-metal implant interface, this time using *in situ* synchrotron tomographic imaging. For this study, titanium screws with or without ZA and BMP-7 were implanted in proximal rat tibiae (N = 15). High-

resolution synchrotron X-ray tomography allowed for the specimens to be imaged during *in situ* pull-out tests, thereby obtaining image volumes with isotropic voxel sizes of 3.6 μm. The pull-out was done incrementally, with steps of 0.05 mm, while being imaged until the fracture of the sample. This *in situ* loading resulted in increased understanding of crack propagation mechanisms and crack types occurring during pull-out. Insight about the mechanical parameters of *in vivo* osseointegrated screws was also gained, concluding that the mechanical resistance of the bone-metal interface did not only depend on the bone formation and used treatment, but also on the parameters of insertion of the screw in the bone, i.e., contact with cortex, distance from the tibial plateau and angulation of the screw. Even though useful insight could be gained through this study, the results were limited by significant image artifacts caused by the interaction of the metal material with X-rays.

The study of *Raina et al.* [6] in 2019, aimed to functionalize a novel hollow PEEK implant that would enhance peri-implant bone formation and implant fixation by adding bioactive molecules (ZA & rhBMP-2) inside a cement-filled core. The novelty of this study is the ability to deliver local drug treatment over time through the design of the implant. In other studies, drug treatments were injected subcutaneously [80] or in the form of putty in the drilled hole in the host bone before the insertion of the implant, causing a reduced amount of drugs to stay around the implant interface once implanted [7, 8]. To achieve this goal, four experimental groups were defined, each group receiving a different dosage or combination of bioactive molecules (N = 44; n = 11 for each group). A calcium sulfate/hydroxyapatite (CaS/HA) carrier providing controlled release of the bioactive molecules filled the hollow design of the implant. Implants were brought into the proximal tibiae of rats (44 male Sprague-Dawley rats). The animal model used in this study is the same as the one used in this Master's degree project and will be further discussed in Section 4.1.2. The methods employed to analyze and validate the peri-implant bone volume formation were radiology, lab-based μCT (isotropic voxel sizes of 10 μm), mechanical testing and histology. Mechanical testing was performed in the form of pull-out tests. The resulting force vs. displacement curves were utilized to draw conclusions about the peak force, stiffness and fracture energy. The main limitation of this study is the use of a single time point to assess the extent of bone formation.

The latest study of *Le Cann et al.* [8] focuses on understanding the more localized, *in situ* deformation of the bone-implant when subjected to loading. Internal displacement and deformation fields were obtained through DVC from images acquired with X-ray μCT (voxel size of $25\mu m$). Four titanium screws were implanted into rat tibiae (N = 4). This study centered around the methodology behind crack propagation and failure patterns of metal implants under loading, as well as assessing the potential of DVC to characterize the properties of newly formed peri-implant bone. An important conclusion from this study is that using DVC, following the *in situ* loading methodology, shows great potential to study internal deformation and fracture behavior of newly formed bone close to an implant during loading. Once again, the small number of specimens used in this study can be considered a limiting factor. The artifacts created by the metal implant during the X-ray tomography also prevents from investigating the finer underlying processes happening at the bone-implant interface during crack initiation and failure.

The mentioned studies focused on comparing bioactive molecules promoting the osseointegration (treated vs. untreated) and investigated peri-implant bone properties and quality with the use of various imaging modalities (X-ray or synchrotron X-ray μCT) and tools (DVC). The implant materials also varied from study to study (metal vs. non-metal).

In this present study, the quality of the newly formed bone around the implant is investigated, using high resolution synchrotron μCT with non-metallic implants. This enables a more detailed analysis of the newly formed bone in the close vicinity of the implant, and better accountability for biological variation within the specimens.

4 Materials and Methods

In this section, the methodology and tools used to assess the bone-implant integration are described. The steps taken to successfully obtain the mechanical properties, conduct bone volume analysis and digital volume correlation (DVC) are presented.

The animal experiment, collection of tibiae specimens and the synchrotron-based imaging experiment concurrently with the mechanical testing were done prior to the start of this degree project (Figure 4.1). The focus in this degree project is thus on data analysis. A more detailed discussion of the analyses will follow in this section. Omitted samples will be discussed in Sections 5 and 6.

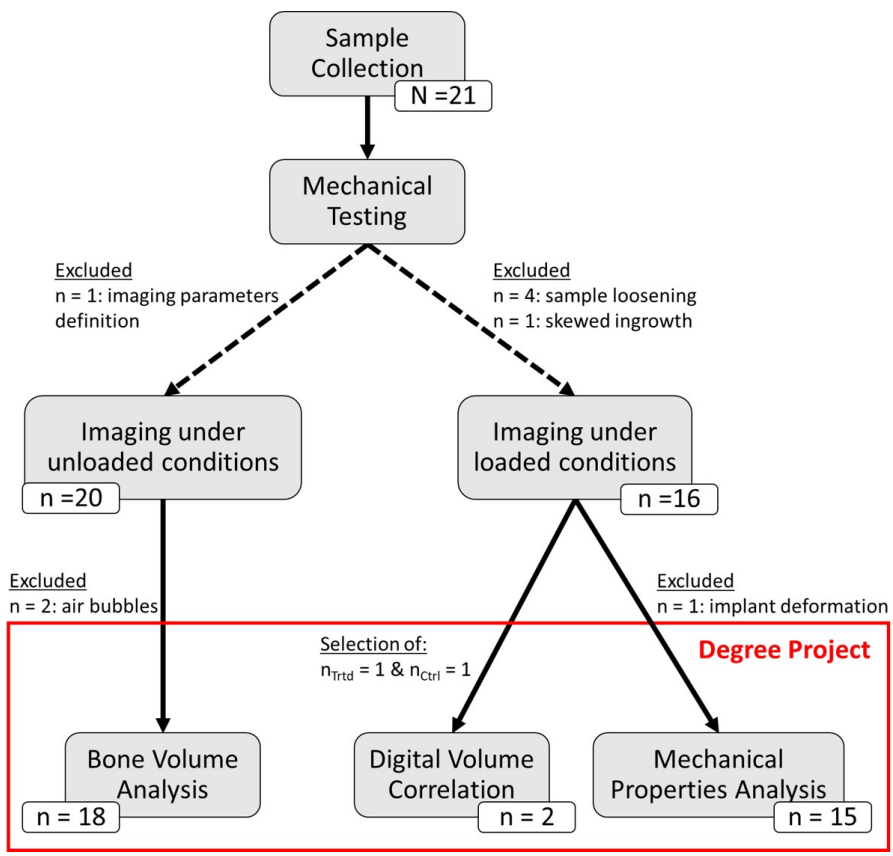

Figure 4.1: The general flow of the conducted experiments, analyses, number of samples used and discarded for each analysis. The parts contained within the red box are the analyses done within this degree project, other parts were done prior to the project.

4.1 Sample Collection

Threaded hollow chamber implants in PEEK (Figure 4.2) were placed in the proximal tibiae of rats (N = 21) and left to integrate for 6 weeks before the tibiae were harvested. The specimens were grouped into a control group (Ctrl, n = 10) where the implants were filled with a biomaterial consisting of 40% hydroxyapatite and 60% calcium sulfate (CaS/HA), and a treated group (Trtd, n = 11) where the implants were filled with a mixture of the biomaterial and bioactive molecules (CaS/HA + rhBMP-2 + ZA) (Figure 4.2C). More details about this animal model can be found in [6].

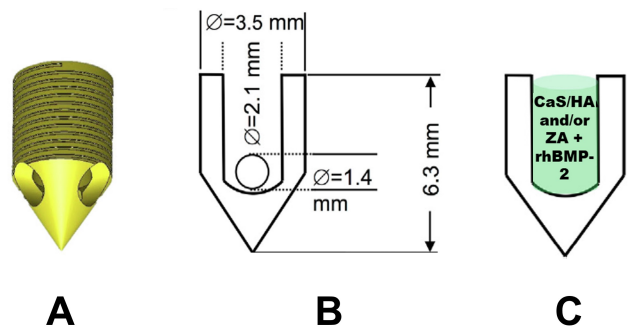

Figure 4.2: Schematic of the PEEK implant. (A) 3D representation of the used PEEK implants. (B) PEEK Implant dimensions. (C)The implants were filled with biomaterial (CaS/HA) or a mixture of the biomaterial and bioactive molecules (CaS/HA + rhBMP-2 + ZA). [Adapted from [6]]

4.1.1 PEEK Implant Design

PEEK is biocompatible and will minimize the amount of imaging artifacts created during X-ray tomography, when compared to commonly used metallic materials [81]. It is a bioinert material and will therefore not releases any harmful components, nor cause adverse reactions with the host bone [82].

The biocompatible PEEK implants consisted of a hollow chamber with a conical base (Figure 4.2A-B). The cylindrical part of the chamber was threaded, and the conical base contained three equally spaced holes at its distal end. The biomaterial CaS/HA, with or without bioactive molecules, was compacted inside the implant (Figure 4.2C). The three equally spaced holes of the triangular end of the chamber allowed for a local delivery of

the bioactive molecules overtime when the CaS/HA material resorbed.

Once the PEEK chamber was implanted in the tibia, the top of the chamber was covered by a biocompatible nylon cap to prevent the ingrowth of fibrous tissue into the chamber, or the protruding chamber threads [6].

4.1.2 Animal Model

Male Sprague-Dawley rats (N = 21; weight at operation: 373 ± 30 g) were procured from Taconic (Denmark). This species of rats showed rapid new bone formation in previous studies [7, 83] and was therefore chosen. The animals were anesthetized using a combination of ketamine hydrochloride (90 mg/kg) and xylazine (12 mg/kg) via the intra peritoneal route and divided amongst the treatment groups in a randomized manner [6].

The surgical site, i.e., the right knee, was shaved and disinfected. A handheld drilling burr (⌀ 3.2 mm) with a pointed tip was used to drill into the cortical bone and the underlying cancellous bone of the tibia, creating a small hole. The implant was then carefully placed in the drilled hole by means of a press-fit manner using a custom-made screwdriver. Approximately 2-3 mm of the threaded part of the chamber protruded from the bone surface so that a connection component could be attached for the subsequent mechanical testing of the specimens. N = 10 animals received an implant filled with only CaS/HA (control) and N = 11 animals received the implant filled with CaS/HA mixed with the bioactive molecules (treated). All implants were left to integrate for 6 weeks before the tibiae were harvested, cleaned, and sectioned before being frozen up until the experiment. Further details about the animal model can be found in [6].

4.2 Mechanical Testing

The quantitative assessment of the implant stability was achieved by investigating the mechanical properties of the bone-implant interface with the use of *in situ* incremental pull-outs of the implants and comparing the results of the control samples with the treated samples. Mechanical properties will give insight about the quality of the bone.

A custom-made loading device with a 500 N load-cell was used. All PEEK samples had a nickel (Ni) bead inserted into the opening of the implant, with the aim of reducing any inwards buckling of the implant during loading. The samples were mounted on a pull-out jig, connected to a load

sensor located underneath the chamber where the samples were placed. A titanium connection piece was screwed onto the protruding implant threads and then connected to a threaded piston in the loading device. By displacing the piston, the implants were pulled out. An overview of the mechanical testing setup can be seen in Figure 4.3.

The loading was done stepwise, in increments of 0.15 mm, until failure, i.e., when the resulting load–displacement curves showed clear post-yield behavior. Parameters for the loading protocol are found in Table 4.1. A pull-out was considered successful when the implant was completely removed from the bone or when there was no apparent deformation of the implant. Conversely, a pull-out was considered unsuccessful when the implant showed deformation or came loose during mounting.

Based on the resulting force-displacement curves, the mechanical characteristics of the bone-implant interfaces, i.e., peak force and displacement, stiffness, and fracture energy were calculated using custom-made MATLAB code.

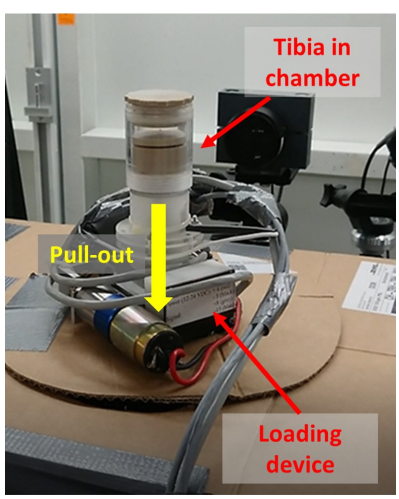

Figure 4.3: The tibia is placed inside the chamber, mounted on the loading device. The X-ray beam comes in from the right, and the detector is placed to the left.

Parameter	**Value**
Pre-load	7 N
Loading rate	0.3 mm/min
Displacement step size	0.15 mm
Sampling rate	2 Hz

Table 4.1: Parameters used for the loading of the implants. The displacement rate of the loading device was determined by the motor voltage.

4.3 Tomographic Imaging

4.3.1 Image Acquisition

The experiments were conducted at the TOMCAT beamline (Swiss Light Source (SLS)[1], Paul Scherrer Institute, Switzerland), which is a synchrotron source, allowing for synchrotron radiation μCT imaging. The specimens were imaged using a monochromatic X-ray beam with an energy of 30 keV. Tomographic images were acquired after mounting of the specimens ("unloaded") and between each loadstep during the pull-out tests, using the parameters detailed in Table 4.2. Using these settings, an isotropic voxel size of 2.75 μm was achieved.

The field of view (FOV) of each scan was 2 mm vertically, thus covering only part of the sample (the tibial implant height was of 6.3 mm). Thus, three sequential scans at different heights were taken at each loading step to cover the entire region of interest (ROI) (Figure 4.4).

The tomographic images were reconstructed in phase contrast mode, after correction using flat-field and dark-field images. The resulting image volumes were 30 Gb in size, contained 1100 image slices of size 2600 x 2600 voxels (i.e., 7.15 x 7.15 mm^2) and were saved in 16-bit (grayvalues between 0 and 65535) TIFF format. Approximately 200 of the image slices overlapped with the subsequent scan.

Table 4.2: Imaging parameters used for tomography acquisition.

Parameter	**Value**
Energy	30 keV
Exposure time	6 ms
Number of projections	3,000
Rotation angle	360°
Scan time (1 scan)	18 sec
Total FOV scan time (3 scans)	54 sec

[1]The Swiss Light Source is a third-generation synchrotron light source where X-rays are produced by a 2.9 T superbending magnet on a 2.4 GeV storage ring [10, 84]

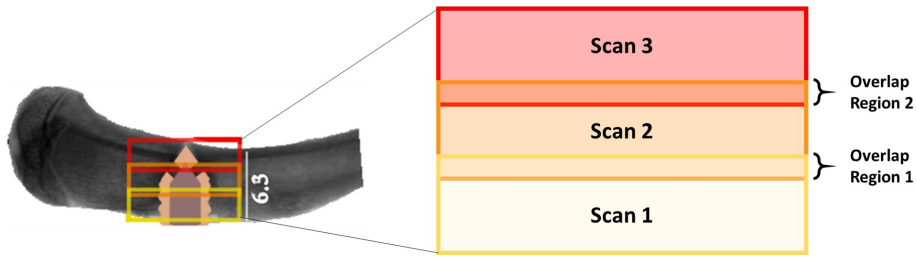

Figure 4.4: FOVs covering the ROI starting at the bottom of the sample chamber (yellow), followed sequentially by mid (orange), and top (red).[Adapted from [6]]

4.3.2 Stitching of the Tomographic Data

The multiple scans that had been acquired to cover the full ROI were stitched to obtain one single image volume.

The stitching was achieved by using in-house MATLAB code (Mathworks, vR2018b). The basic steps were as follows:

Step 1: Load the first image (A) of the second image volume (Scan 2 in Figure 4.5).

Step 2: Load a range of images (B), in the first image volume (Scan 1 in Figure 4.5). This range should include a match for (A).

Step 3 (Optional): Apply a Gaussian filter (*imgaussfilt* [85]) with $\sigma = 1$ if the noise in the images prevented the correct identification of best match (Step 4) in a previous stitching attempt.

Step 4: Find the best match for A in B (Image C in scan 1) by calculating the minimum difference between A and every image in B. In scan 1, a new overlapping region is then defined starting from the matching image C in B, until the end of scan 1. In scan 2 the overlapping region includes the same number of images as the overlapping region in scan 1 but counting from the start of scan 2.

Step 5: Take the mean of the overlapping regions of scan 1 and 2 and export the combined volumes as one new volume.

The steps are repeated to stitch all scans covering the full ROI. During the second iteration, the first image volume will be the newly stitched stack from the previous iteration, and the second image volume will be scan 3. Fully stitched images volumes consisted of 2902 images of 2600 x 2600 voxels.

To validate the success of the stitching process, the new image volume created in Step 5 was visualized using ImageJ (ImageJ 1.52p [86]). A representative successfully stitched image is shown in Figure 4.6.

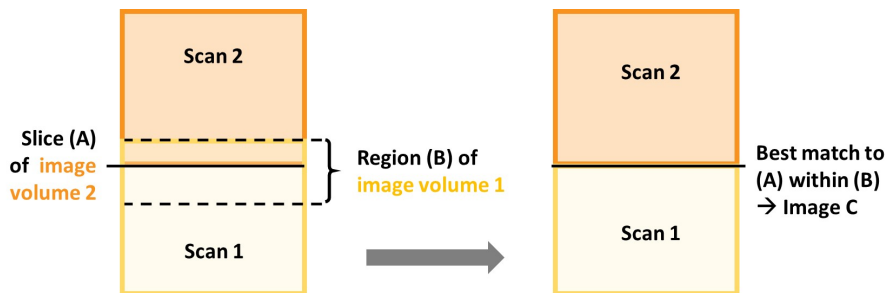

Figure 4.5: Overview of the stitching process of the custom-made MATLAB script, used to stitch two subsequent substacks into one final stack.

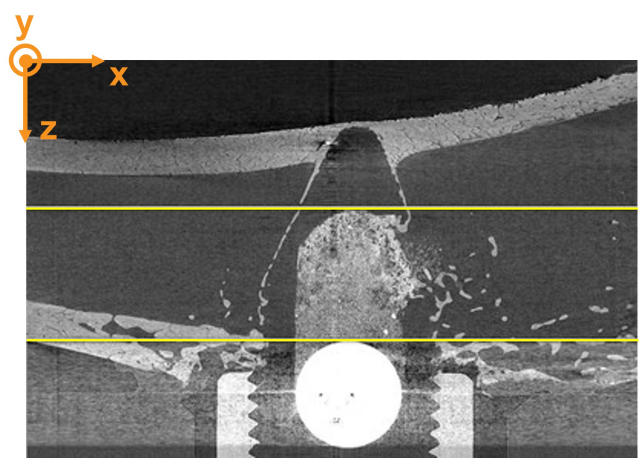

Figure 4.6: Tomographic image slice of a PEEK implant in the tibia. The image was created using the MATLAB script stitching protocol to stitch three scans onto one. The yellow horizontal lines correspond to the edges of the lower and middle images for which best matches were found.

4.4 Bone Volume Analysis

The quality of the bone-implant integration was quantified using the X-ray CT data to visualize the newly formed bone around the implants and quantify the bone volume fraction (BV/TV).

4.4.1 Image Pre-processing

Bone ingrowth volume was calculated from the stitched image volumes from the unloaded scans using CTAn (v1.16.1.0, Skycan, Belgium). As CTAn can only perform a bone volume analysis on BMP images, the TIFF images were converted to 8-bit BMP images (grayscale images with values ranging from 0 to 255) by using in-house MATLAB code.

Using ImageJ, all image volumes were re-aligned through rotation of the images to have the axis of the implant be oriented parallel to the vertical Z-axis (Figure 4.6).

4.4.2 Definition of the Regions of Interest

The ROIs were defined manually in CTAn to match the ROIs described by *Raina et al.* [6], i.e., starting from the top of the holes of the implant and extending 1.5 mm towards the tip.

The image slice at which the holes started was identified manually using ImageJ. The image volumes were firstly sliced along the XZ-plane (See Figure 4.7A). From the resulting stack (Figure 4.7B), the starting slice height of the holes was identified by visual inspection.

When defining the BV/TV, the cortical bone of the sample should not be considered. A first step towards defining the BV/TV was thus to manually mask the cortex of every sample using CTAn, keeping only the image regions containing trabecular bone, peri-implant bone and the implant itself. To achieve this masking, the cortical bone present in the image slice at the height of the chamber holes was masked manually. The same was done for the image slice 1.5 mm below this slice and interpolation was used for all slices in between.

Next, a circular ROI (⌀ 4 mm) was drawn on the image slice where the top of the chamber holes was identified. Another circular ROI (⌀ 2.5 mm) was then drawn on an image slice 1.5 mm below the first. Interpolation between these two ROIs created a truncated cone shaped ROI (ROI_{Outer}) that followed the triangular geometry of the implant head (Red ROI in Figure 4.8).

The second ROI, the inner ROI (ROI_{Inner}), followed the same design methodology as used for ROI_{Outer}, but using smaller diameters as to exclude the volume of the implant and its internal content (CaS/HA remnants) (Blue ROI in Figure 4.8). The circular ROI at the top of the

chamber holes had a diameter of 3.2 mm and the circular ROI defining the other extremity had a diameter of 2 mm. Excluding ROI_{Inner} from ROI_{Outer} created a ROI (ROI_{BVTV}) extending 0.8 mm from the surface of the implant (Area between the red and blue ROI in Figure 4.8).

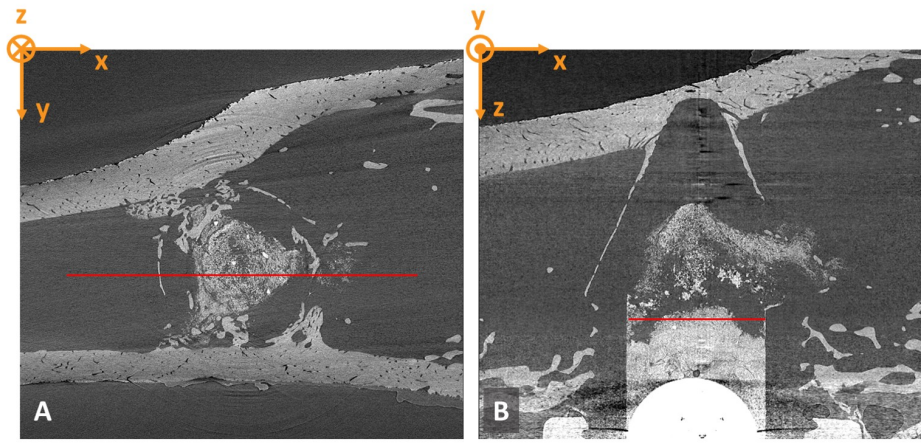

Figure 4.7: Slicing and identification of the start height of the chamber holes of a specimen. (A) Red line representing the slicing direction along the XZ-plane. (B) Resulting sliced view of the implant in the XZ-plane. The red line indicates the start of the holes of the chamber.

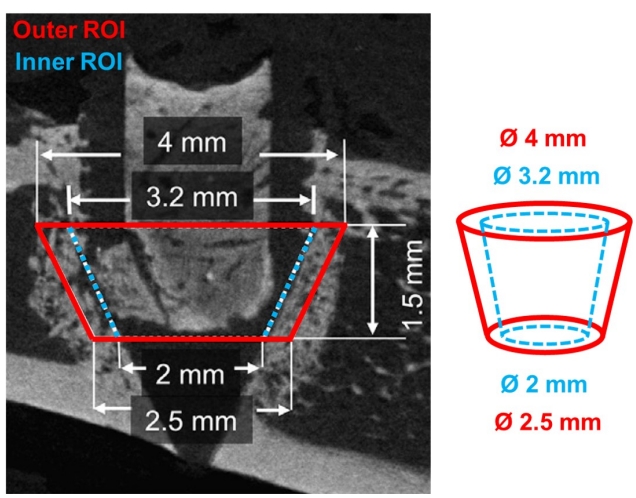

Figure 4.8: The region of interest (ROI) used for the BV/TV calculations was defined by two ROIs; the outer and inner ROI, which are illustrated in red and blue respectively. [Adapted from [6]]

4.4.3 BV/TV Calculation

As the BV/TV looks at the bone volume (BV) between the inner and outer ROI, bone was segmented using a threshold of 115, determined by visual examination of the 8-bit BMP image volumes of all samples. This threshold was used for all image volumes and allowed to remove noise present in the images whilst keeping enough detail of the trabecular bone structures.

Using CTAn, BV and TV were obtained for all specimens (Figure 4.9). The BV/TV was then calculated.

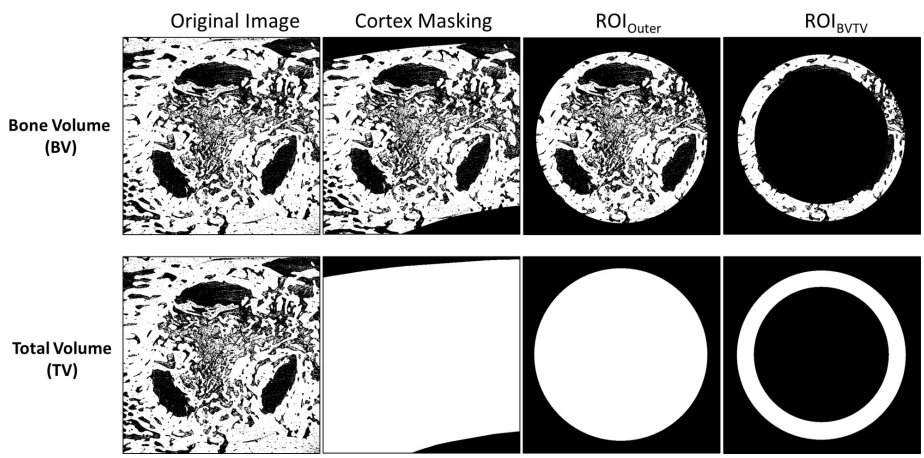

Figure 4.9: Overview of the ROI application process. ROI$_{Outer}$ contains the bone formed immediately around the implant as well as bone and CaS/HA inside the implant. In ROI$_{Inner}$ the material inside the implant has been removed. For the Bone Volume (BV) and Total Volume (TV) calculation, a 3D analysis was performed in CTAn on the stack of ROI$_{BVTV}$ binary images.

4.5 Digital Volume Correlation

One specimen of the treated group and one specimen of the control group were selected for further internal strain analysis using DVC to identify regions of bone cracking and deformation. The selection of the representative samples was based on the loading curves resulting from the mechanical testing. Samples that failed after more than three loadsteps and showed a clear drop in the force-displacement curve, indicating failure, were selected as representative samples of their respective treatment groups.

The scans taken during the three final loadsteps were used for DVC to

analyze the strain and force displacement fields in each representative sample.

Additionally, the image volumes of both selected samples were visually analyzed in ImageJ to confirm that significant cracks, fractures and deformations occurred within the final loadsteps prior to fracture.

4.5.1 Image Pre-processing

To reduce the computational cost of DVC analysis on full image volumes, the 2902 16-bit (2600 x 2600 voxels) phase contrast images were binned twice using in-house MATLAB scripts, resulting in 650 bin 4 image volumes of size 650 x 650 voxels.

Binning refers to the combination of voxels into bigger voxels. When binning the original (bin 1) images to bin 4 images, a 4x4x4 cube of 64 neighbor voxels is combined into 1 single voxel (Figure 4.10), thereby downscaling the images. Resulting image stacks contained 650 cross-sectional images of 650 x 650 pixels and were eventually cropped to cross-sectional images of 550 x 550 pixels to reduce the size of the stacks.

Next, to further reduce the computational cost of the DVC analysis on the image volumes, images containing the Ni beads were removed from each stack. For each stack, the slice at which the top of the bead became visible was identified by visual identification in ImageJ and all the subsequent slices were removed. The Ni bead created metal artifacts during the tomographic imaging, preventing a clear visualization of the bone and therefore also limiting the acquisition of useful information. Additional slices could be removed to ensure that after the bead removal, stacks of a same sample had identical lengths.

The original and binned images were filtered using a despeckling filter (ImageJ *Despeckle*) and a Gaussian blur filter with $\sigma = 3$ (ImageJ *Gaussian blur*). To mask away the background and internal voids, a threshold value was identified by manual inspection of the images. Examination of representative cross-sections within each stack revealed that the bone tissue fell between voxel intensity values of 28559 and higher. By thresholding the filtered bin 1 (original size) and bin 4 images in ImageJ (ImageJ *Threshold*), a mask was obtained, which was then applied to the original bin 1 and bin 4 μCT images, respectively (See e.g., Figure 4.11).

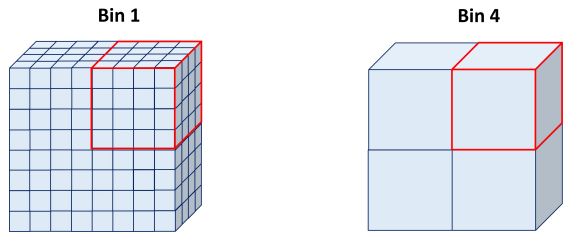

Figure 4.10: Overview of the process of binning 64 voxels into one single voxel.

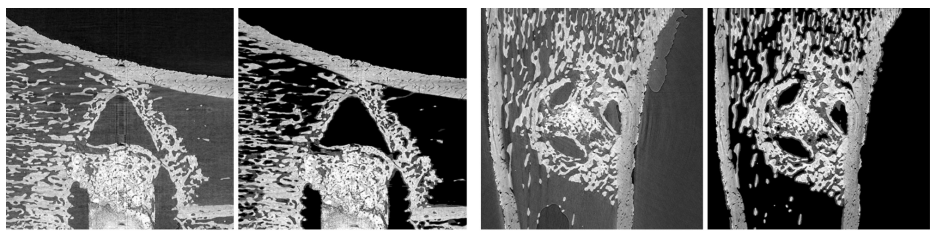

Figure 4.11: Removal of the voids and background voxels in image volumes by the application of a mask, obtained through thresholding, i.e., setting all grayvalues below 28559 to 0 (black).

4.5.2 DVC Analysis

The python-based software TomoWarp2 [76] was used to do incremental DVC for the stitched images from the 3 loadsteps prior to failure for each specimen.

Prior to the DVC analysis, a visual analysis of the high-resolution images was performed in ImageJ, thereby identifying locations of clear bone fracture and deformation. For each sample, two ROIs of 100 x 270 x 310 voxels in the original bin 1 images (i.e., 25 x 68 x 78 voxels for bin 4 images) of the last loadstep before failure were identified. Each ROI contained a different type of crack. One ROI contained a larger crack opening (i.e., $>$ 10 pixels or 27.5 μm), and one a smaller crack opening ($<$10 pixels) (Figure 4.12). This allowed for the evaluation of the efficiency of DVC to detect finer and coarser cracks using image volumes of different resolution (bin 4 and bin 1 images).

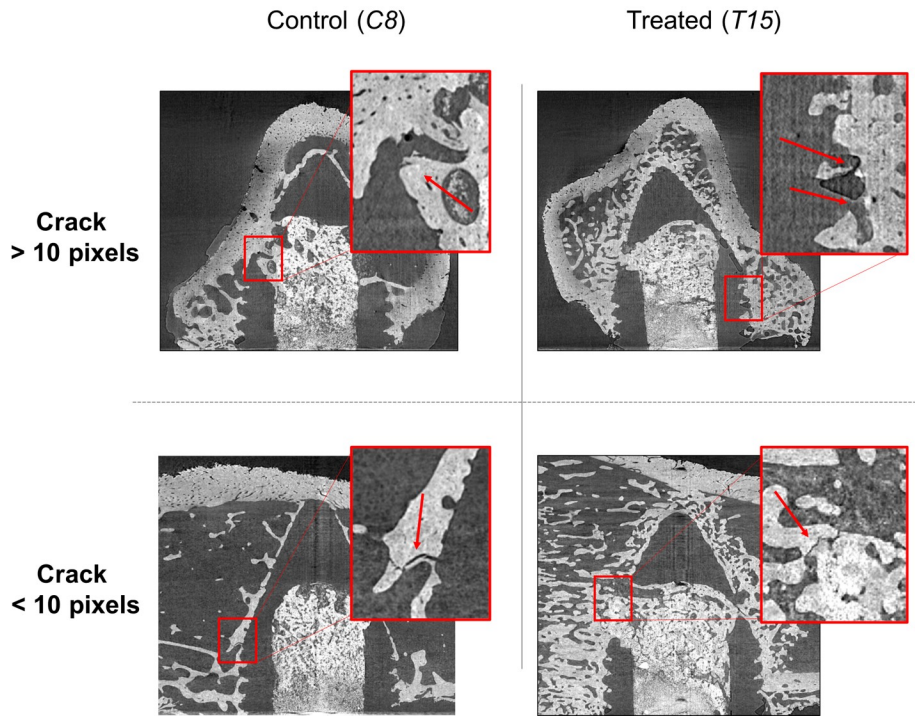

Figure 4.12: Cracks selected for the DVC analyses of the representative samples of the control and treated groups (*C8* and *T15*). The cracks are indicated by the red arrows. The first and second rows contain the selected larger ($>$ 10 pixels) and finer ($<$ 10 pixels) crack, respectively.

In a first DVC analysis step, the input parameters, i.e., SW, CW, and NS were defined. To define the SW for the first DVC analysis on bin 4 images, the beadless bin 4 image volumes of the last loadstep (step 3) and next-to-last loadstep (step 2) of both selected samples were visually analyzed in ImageJ. This analysis allowed to assess expected displacements in all directions of different bone structures, thereby defining the 3D range of the SW. The NS and CW were defined through trial and error, by finding a right balance between having enough resolution (small NS) in the resulting displacement and strain fields and having enough variance in grayvalues inside the CW, while keeping the computational cost low and obtaining high correlation coefficient values (See also Figure 4.13). Limiting the variance of grayvalues within the CW too much can cause the CW in the original image to match with a lot of different sub-volumes, in different locations of the deformed image.

For both samples, a cubic search window (SW) of ±25 voxels, and a correlation window (CW) of ±5 voxels were defined, centered around the node. A node spacing (NS) of 10 pixels was used (Table 4.3).

As the image volumes were thresholded during the pre-processing steps (See Section 4.5.1), a value of the threshold needed to be defined as additional DVC input parameter. Half of the threshold value used to mask the background in the pre-processing step (28559) was set as a lower threshold for the DVC analyses, i.e., 14279). This means that if the mean grayvalue inside the correlation window (CW) is lower than this 14279 value, the analysis on the corresponding node will not be carried out. This is used to reduce the computational time by skipping nodes falling in voids, as a CW containing a majority of black void voxels will automatically fall below the 14279 threshold value. Contrarily, a CW containing a few void voxels will have a mean voxel value that will fall below the bone-segmentation threshold value of 28559, but above the lower threshold value of 14279, and therefore not be discarded from correlation.

Once all the parameters were set, a first DVC analysis was performed on the bin 4 image volumes of the representative treated and control sample, with a CC-interpolation subpixel mode. Using the same parameters, a subsequent DVC was run on these same image volumes, using the image-interpolation mode. This run reprocessed a subset of nodes for which the previous correlation did not give satisfactory results. The displacement fields derived from this second DVC analysis were filtered by removing outliers (points whose values diverged more than double from the median value of their surrounding points; $\varnothing = 1$) and applying a 3D median filter ($\varnothing = 1$). The strain fields were then calculated based on the filtered displacements.

Once the DVC was run on the bin 4 images of loadsteps 2 and 3, the displacement fields were firstly analyzed. This was done to check if the calculated 3D displacement ranges matched the expected ranges of displacements. To obtain a better overview of the displacements, the individual X-, Y-, and Z-displacement fields were combined into a single field by calculating the displacement magnitudes of each node.

If the expectation matched the calculated displacements, and if the average correlation coefficient of the analysis lay above 97% [9], then the DVC analysis was considered successful and the strain fields within the ROIs were investigated.

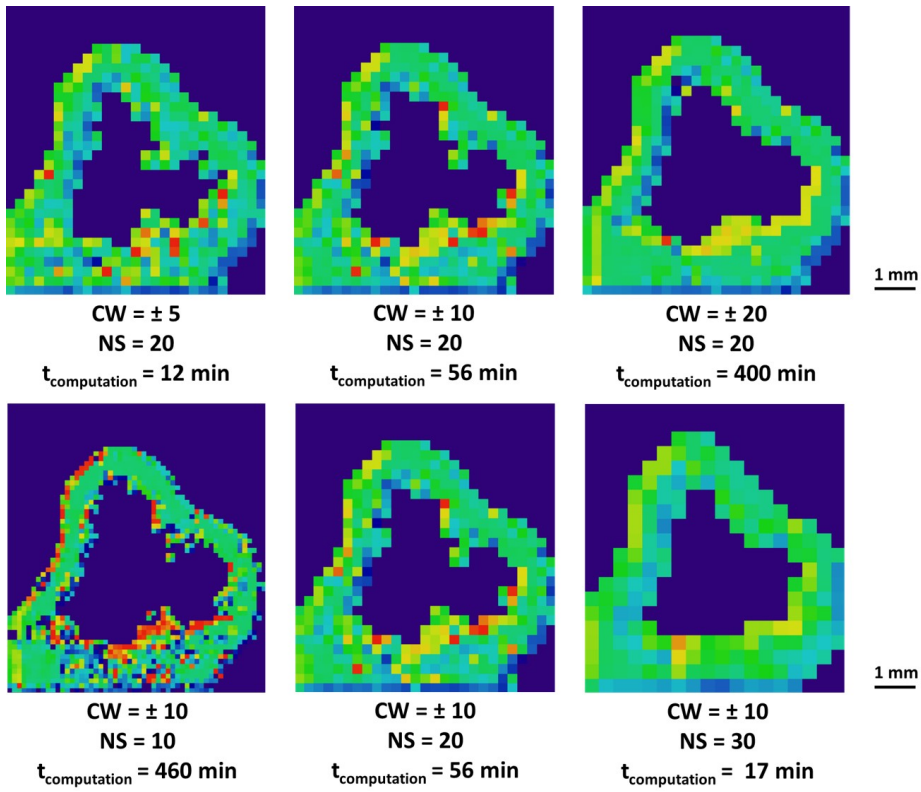

Figure 4.13: The effect of the correlation window and node spacing input values on the resolution of strain maps and the computation time. The search window size stayed the same for all cases, i.e., ± 25 pixels. The lower parameters result in strain maps with higher definition.

When the strain fields showed significantly high compressive and/or tensile strain in the regions of the cracks under analysis, a new DVC analysis was performed on the images of the previous loadsteps, i.e., steps 1 and 2. Step 1 refers to the antepenultimate loadstep before failure. This new DVC analysis was done on the bin 4 images of loadsteps 1 and 2, using the same CW, NS, and SW as for the analysis of loadsteps 2 and 3. The resulting strain and displacement fields inside the different ROIs were once again visually analyzed and compared to their respective CT images. This enabled to check for the presence of damage in the high-strain regions in these earlier loadsteps, thereby evaluating if DVC could be used to identify damage that was maybe not clearly noticeable during the visual examination of the μCT images.

To push this evaluation of DVC as a bone damage identification tool a bit further, DVC at higher resolution was performed on the bin 1 image volumes of loadsteps 1 to 3. Instead of conducting a full image volume analysis, only the voxels inside the previously identified ROIs were analyzed. The input parameters used were CW = ± 2.5 voxels, NS = ± 5 voxels, and SW = ± 30 voxels (Table 4.3). By using this CW and NS, high resolution strain and displacement fields were obtained. Using a bigger CW and NS, e.g., ± 5 pixels and 10 pixels respectively, made it more difficult to identify the cracks due to the lower resolution of the output fields. Using a smaller CW and NS would limit the variance of grayvalues within the correlation window too much.

The resulting high-strain and damage locations of the control and treated sample were compared with each other, and with the qualitative results of previous studies using DVC for bone analysis [6, 7, 8, 10].

Table 4.3: Input parameters used for Digital Volume Correlation analyses on bin 1 and bin 4 image volumes.

	Bin 4	**Bin 1**
Correlation window (pixels)	± 5	± 2.5
Node spacing (pixels)	10	5
Search window (pixels)	± 25	± 30

4.5.3 DVC Error Quantification

To define the accuracy and precision of the DVC measurements, the errors on the calculated displacement and strain components were defined for the high-resolution bin 1 images volumes, and the downscaled bin 4 image volumes. To that end, a DVC analysis was performed using an unloaded image stack of one of the selected specimens, and its virtually translated copy, as input image volumes. A virtual translation of 2 pixels in the X-, Y-, and Z-direction was applied for the bin 4 and bin 1 image volumes. The same DVC input parameters as mentioned in Table 4.3 were used for these analyses (Section 4.5.2).

Once the DVC analysis completed, the mean (accuracy) and standard deviation (precision) were calculated of the resulting absolute values of the X-, Y-, and Z-displacement components, as well as for all six strain components (i.e., the 3 normal strain and 3 shear strain components) in every node.

4.6 Statistical Analysis

Mean values (μ) and standard deviations (SD) were calculated for all the values derived from the microstructural (BV/TV), mechanical and DVC analyses for each treatment group. A Mann-Whitney U Test was performed to compare the results for the treated and control group. Linear regression analyses were performed between the mechanical properties and the bone volume fractions. The coefficient of determination (R^2) and coefficient of Spearman (ρ) were defined for those correlations. When calculating the correlations, the data of both treatment groups were merged. For all analyses, $p < 0.05$ was considered statistically significant.

5 Results

In this section, the results obtained from the pull-out tests, and image analyses (BV analysis and DVC) are presented. The collected tibiae samples were numbered from 1 to 21 and denoted with the prefix *C* for the untreated control samples (*C1-C10*) and *T* for the treated samples (*T11-T21*).

5.1 Mechanical Testing

Pull-outs were performed on 16 of the 21 samples. Five unsuccessful pull-outs were excluded from the analysis, two due to implant loosening during mounting of the samples on the pull-out jig (*C6, C7, T17*), one due to implant loosening during the pre-loading step of the mechanical testing (*T20*), and a final one due to the implant's ingrowth angle in the host bone (*T16*). The implant angle of this last specimen caused incorrect contact between the bone and the "floor" of the loading device, which caused the specimen to rotate during the first load steps rather than the implant being pulled out. Therefore, no loading data was available for sample *T16*. Additionally, sample *C7* was used to define the imaging parameters of the imaging modality, thereby receiving radiation doses exceeding the limit value of 35 kGy (Section 3.3.2), making it unreliable for any further mechanical analysis.

During the pull-out testing, 2 samples slipped (*C1* and *C9*), making their measured peak force, peak displacement, and fracture energy unreliable. For those samples, only the stiffness is considered. The mechanical data of sample *C3* was completely omitted due to implant deformation during the pull-out tests.

The force-displacement curves for the 16 tested samples show an overall increase in peak force and peak displacement for the samples of the treated group (Figure 5.1).

The mean (μ) and standard deviation (SD) for the control and treated group, for the peak force (N), peak displacement (mm), stiffness (N/mm), and fracture energy (J/mm^2) are presented in Table 5.1. According to the statistical analysis no significant differences were observed between the mechanical parameters of the control and treated group. However, an overall increase of the mechanical parameters was notable. In the treated group, four samples reached a peak force that was higher than

100N, thereby exceeding the maximum peak force measured in the control group.

Statistically significant correlations were found between the fracture energy and peak displacement ($R^2 = 0.67$; $\rho = 0.82$), and peak force ($R^2 = 0.50$; $\rho = 0.81$). Peak force also correlated significantly with stiffness ($R^2 = 0.59$; $\rho = 0.72$)

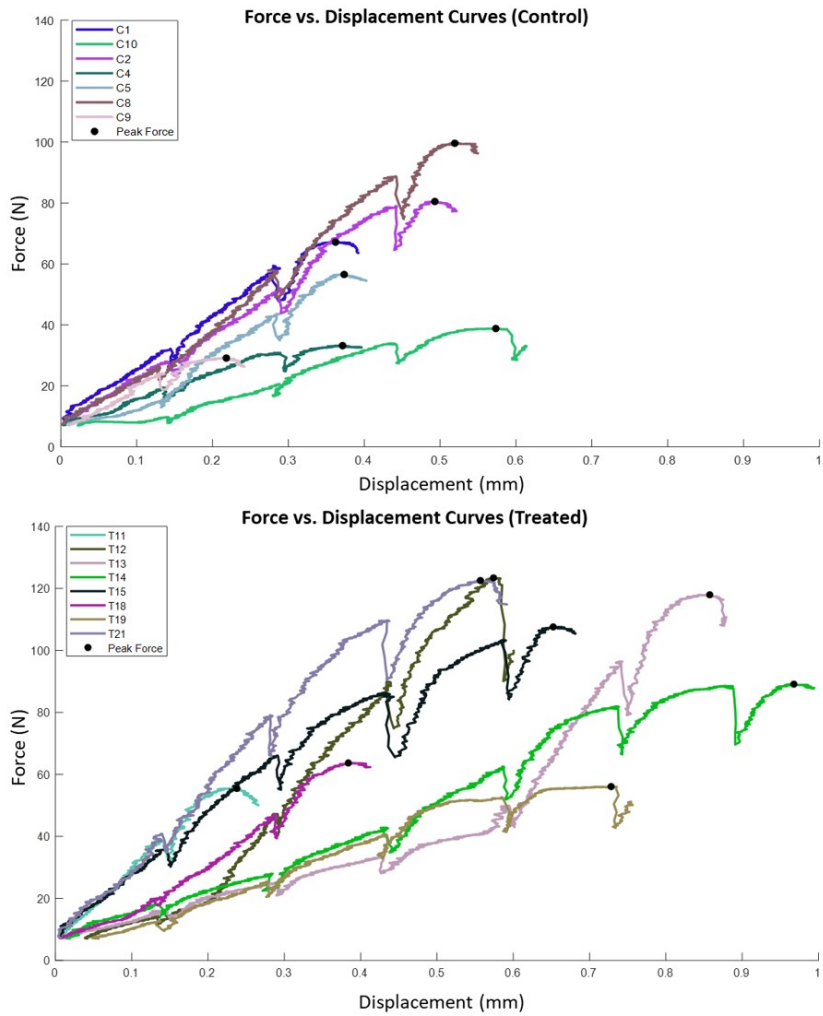

Figure 5.1: *In situ* pull-out load curves of the control (Top) and treated (Bottom) samples, plotting the loading force (F) in function of the implant displacement (mm). The peak force for each sample is indicated by a black marker.

Table 5.1: Overview of the mechanical bone-implant properties of the control and treated group, calculated from the data of the pull-out tests. The respective increases of the mean values of all mechanical parameters show an overall improvement for treated implants compared to controls. The respective p-values were calculated and show that there is a significant increase in fracture energy for the treated group.

Sample	**Peak Force (N)**	**Peak Displacement (10^{-2} mm)**	**Stiffness (N/mm)**	**Fracture Energy (J/mm^2)**
		CONTROL		
C1			172.6	
C2	80.5	49.3	164.5	22.1
C4	33.2	37.1	91.2	8.0
C5	56.5	37.4	150.7	10.3
C8	99.6	51.9	217.7	26.8
C9			111.9	
C10	38.8	57.3	88.7	12.2
$\mu\pm$***SD***	61.7±28.1	46.6±9.0	142.5±44.0	15.9±8.1
		TREATED		
T11	55.5	23.8	242.6	7.8
T12	123.4	57.4	289.5	29.4
T13	117.9	85.7	374.5	37.8
T14	89.1	96.8	110.8	48.0
T15	107.6	65.2	207.8	41.7
T18	63.7	38.4	178.1	12.0
T19	56.1	72.8	94.1	23.6
T21	122.6	55.7	261.5	39.7
$\mu\pm$***SD***	92.0±29.9	62.0±23.8	219.9±87.0	30.0±14.5
Change of μ	49.0% (p = 0.13)	33.0% (p = 0.13)	54.3% (p = 0.07)	88.7% (p = 0.13)

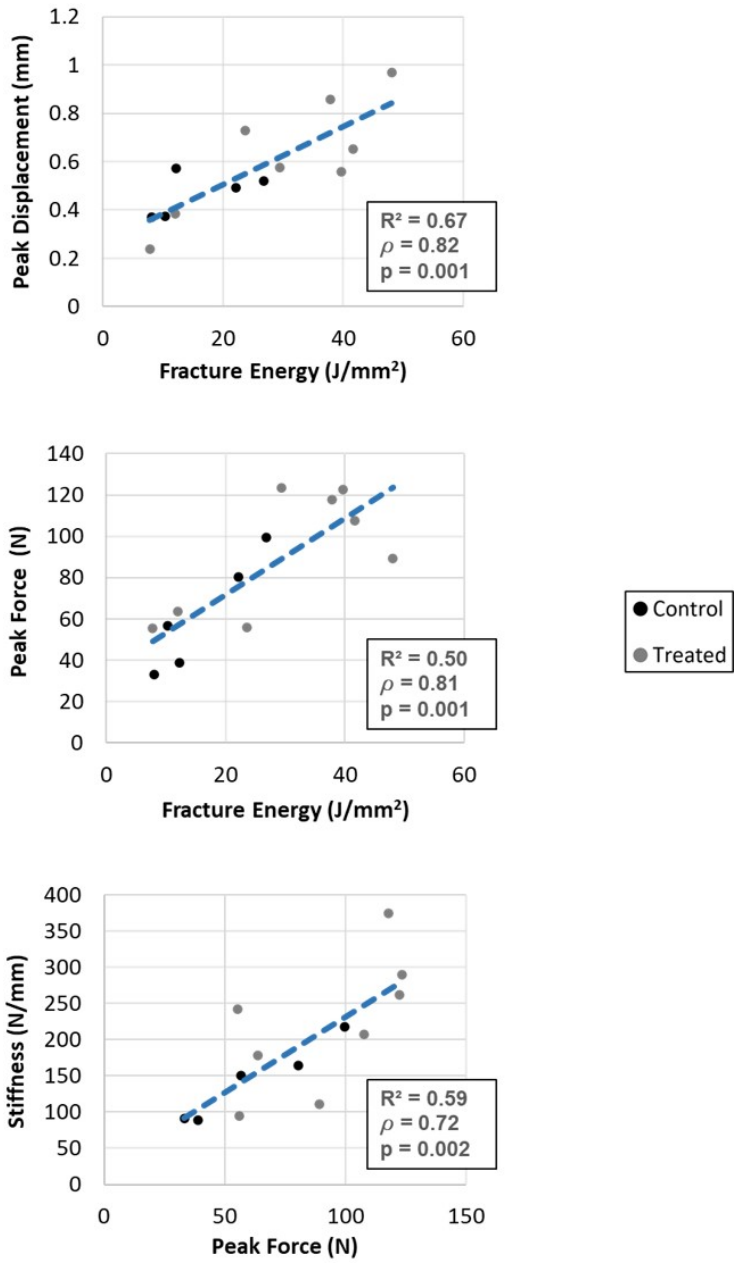

Figure 5.2: Significant ($p < 0.05$) correlations obtained between the different mechanical properties, i.e., peak displacement, peak force, fracture energy and stiffness, are shown with their respective Spearman correlation coefficient (ρ) and R^2 value of linear regression curve. The linear regression curve is represented in blue.

5.2 Bone Volume Analysis

The bone volume (BV), total volume (TV) and bone volume fraction (BV/TV) were calculated for each sample and the results are presented in Table 5.2. Higher BV/TV values were found in the ROI defined around the implants of the treated group (51.73% ± 15.31%) compared to the ones from the control group (14.76% ± 5.74%) (p = 0.0005).

Samples *T17* and *T20* were omitted from the bone volume analysis. The μCT images of both samples *T17* and *T20* indicated the presence of air bubbles inside the screw and at the bone-implant interface, which made it impossible to correctly define the amount of bone present around the implant inside the defined ROI.

Correlations were calculated between the obtained trabecular BV/TV values and the mechanical properties of Section 5.1 (Figure 5.3). Significantly high correlations were found between BV/TV and fracture energy (R^2 = 0.68; ρ = 0.81; p = 0.001), and between BV/TV and peak displacement (R^2 = 0.43; ρ = 0.74; p = 0.004), while no significant correlation was found between BV/TV and stiffness (p = 0.49). Peak force showed low correlation with BV/TV (p = 0.17).

Table 5.2: Sample characteristics. Samples from the treated group showed a significant average bone volume fraction increase of 221.23% compared to the samples of the control group (p = 0.001).

Sample	**Bone Volume (mm^3)**	**Total Volume (mm^3)**	**BV/TV (%)**
	CONTROL		
C1	0.65	3.66	17.71
C2	0.61	4.16	14.67
C3	0.32	3.79	8.33
C4	0.35	4.15	8.44
C5	0.58	4.25	13.73
C6	0.37	4.46	8.27
C8	0.76	3.94	19.27
C9	1.24	7.05	17.57
C10	1.05	4.20	24.89
$\mu\pm$***SD***	0.66±0.32	4.41±1.02	14.76±5.74
	TREATED		
T11	0.72	4.45	16.14
T12	1.81	3.54	51.23
T13	1.65	3.52	46.88
T14	2.46	4.44	55.34
T15	2.68	4.47	59.87
T16	3.00	4.19	71.55
T18	2.17	4.18	52.01
T19	2.65	4.27	62.21
T21	1.88	3.73	50.31
$\mu\pm$***SD***	2.11±0.69	4.09±0.39	51.73±15.31
Change of μ	+221.23% (p = 0.0003)	-7.24% (p = 1)	+250.35% (p = 0.0005)

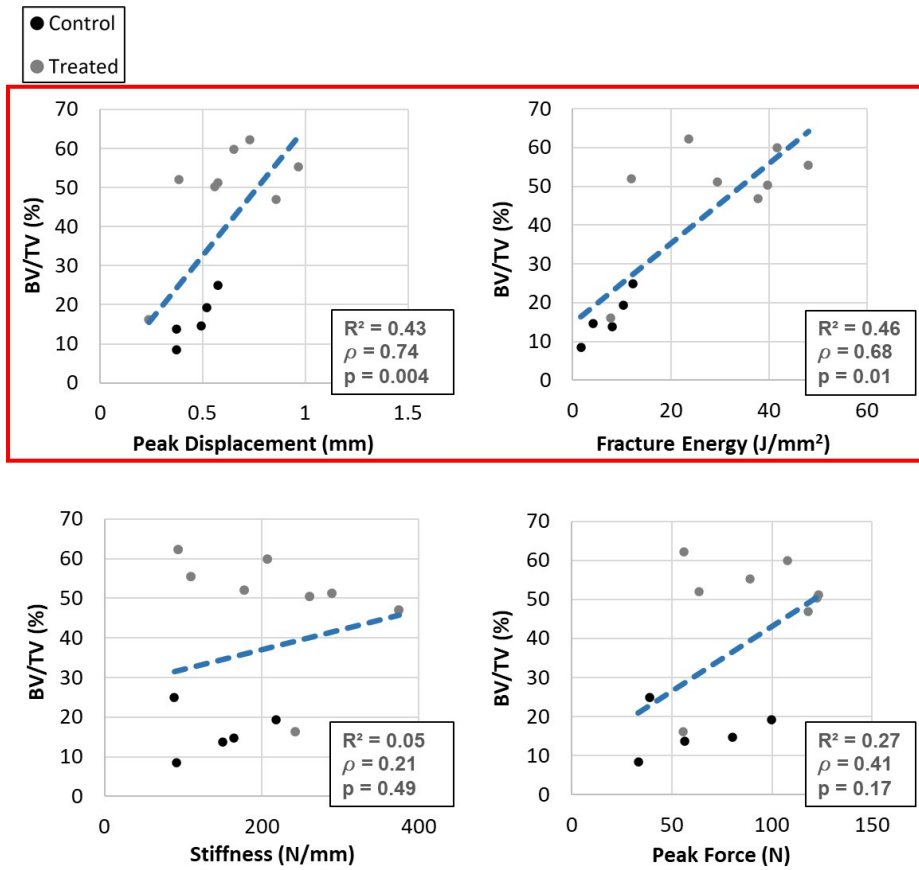

Figure 5.3: Correlations obtained between the different mechanical properties, i.e., peak displacement, peak force, fracture energy and stiffness, with BV/TV are shown with their respective Spearman correlation coefficient (ρ) and R^2 value of linear regression curve. The linear regression curve is represented in blue. Significant ($p < 0.05$) correlations are indicated by the red box.

5.3 Digital Volume Correlation

Sample *C8* was chosen as representative sample for the control group, whereas sample *T15* was selected for the treated group. Their mechanical and BV/TV parameter values showed consistent resemblance to the calculated mean values of their respective groups. Both samples also showed regions with significant cracking and deformation.

5.3.1 Error Quantification

The uncertainties in the DVC displacement and strain measurements were calculated for the downscaled (bin 4) and high-resolution (bin 1) μCT images (Table 5.3). To easily compare these errors with other studies who applied different displacement values and worked with different image resolutions, the errors were expressed in pixels. Additionally, the percentage errors were calculated to put the errors in perspective and allow easier comparison with previous studies (Table 5.4).

The average uncertainties for the DVC displacement measurements were 0.07 $\pm$ 0.46 pixels for the DVC performed on bin 4 images, and 0.03 $\pm$ 0.12 pixels for DVC performed on bin 1 images.

The highest strain error was found for the DVC performed on bin 4 image volumes (12800 $\pm$ 51900 $\mu\epsilon$).

Table 5.3: Accuracy (mean) and precision (standard deviation) were defined for the 3D displacement and strain components for bin 4 and bin 1 image volumes.

	Bin 4		**Bin 1**	
	Accuracy	Precision	Accuracy	Precision
X-disp. (pixels)	0.050	0.407	0.006	0.019
Y-disp. (pixels)	0.061	0.261	0.021	0.315
Z-disp. (pixels)	0.094	0.714	0.001	0.028
Strain ($\mu\epsilon$)	12 800	51 900	977	602

Table 5.4: Fractional error values (in %) were obtained by dividing the accuracy of each displacement direction by the applied displacement of 2 pixels.

	Bin 4	**Bin 1**
X-displacement	2.5%	0.3%
Y-displacement	3.1%	1.1%
Z-displacement	4.7%	0.1%

5.3.2 Displacements and Strains

Similar results were observed for both analyzed samples in terms of crack initiation and failure modes. Both samples showed significant cracking at the threads of the implants and in the thin, newly regenerated peri-implant trabecular bone.

The first DVC analyses were conducted on the final loadsteps of the bin 4 image volumes of *C8* and *T15* with good correlation (average correlation coefficient (CC) of 97.9 ± 3.7%). Resulting displacement, and strain fields of these analyses are shown in the second column of Figures 5.4 - 5.7.

For the control sample, a clear displacement gradient was noticeable inside the local ROI containing the larger crack (Figure 5.4(B.2)), expressing high strains which were visible in Figure 5.4C.2. This was not the case for the displacement field of the finer crack identified in the control sample (Figure 5.5(B.2)). High strains were visible at the edges of the bone region inside the ROI with the fine crack (Figure 5.5(C.2)). Finer cracking was thus not detected by the DVC for the bin 4 images.

For the treated sample, the ROI containing the bigger crack showed a slight color gradient at the bone edge for the displacements (Figure 5.6(B.2)). No significant color gradient was identified inside the ROI containing the smaller crack (Figure 5.7(B.2)). Cracking in this sample was not well detected by the DVC for the bin 4 images.

Next, the previous loadsteps (steps 1-2) were analyzed using the same input parameters as for steps 2-3. As for both the treated and control samples, no significant gradient in displacement and strain values was detected during the DVC analysis of step 2-3 for the ROI containing the smaller crack, this second DVC analysis was only carried out on the ROI containing the bigger crack (Figures 5.4 and 5.6, left column).

This time, for both samples, weak gradients were found within the ROIs, for the displacement and strain fields (Figures 5.4 and 5.6 (B-C)). The CT images for the respective ROIs also showed small cracks in those areas (Figures 5.4 and 5.6(A)).

Finally, by performing a DVC analysis on the high-resolution bin 1 image volumes, and consequently zooming in on the defined ROIs containing the small and large cracks, higher resolution displacement and strain fields were obtained (Figures 5.8 and 5.9). A good correlation was obtained for the bin 1 analysis (average correlation coefficient of 98.7 ± 3.5%).

For the control sample, the resulting displacement fields for both cracks over the three loadsteps (Figures 5.8B and 5.9B) showed steep color gradients in the regions were cracking was previously identified in the CT images (Figures 5.8A and 5.9A). These fields match well with the gradients identifiable in the strain fields of the bigger crack (Figure 5.8C).

For the treated sample, the displacement fields for the big crack over the three loadsteps (Figure 5.10B) also showed steep color gradients in the regions were cracking was previously identified in the CT images (Figure 5.10A). In the displacement magnitude field of the final loadsteps (Step 2-3) of the finer crack, however, a lot of different color gradients were present in the area around the previously identified crack (Figure 5.11B). In the displacement field output from analyzing Step 1-2, steep displacement is shown where no crack was yet noticeable in the CT images of step 1 and 2 (Figure 5.11A).

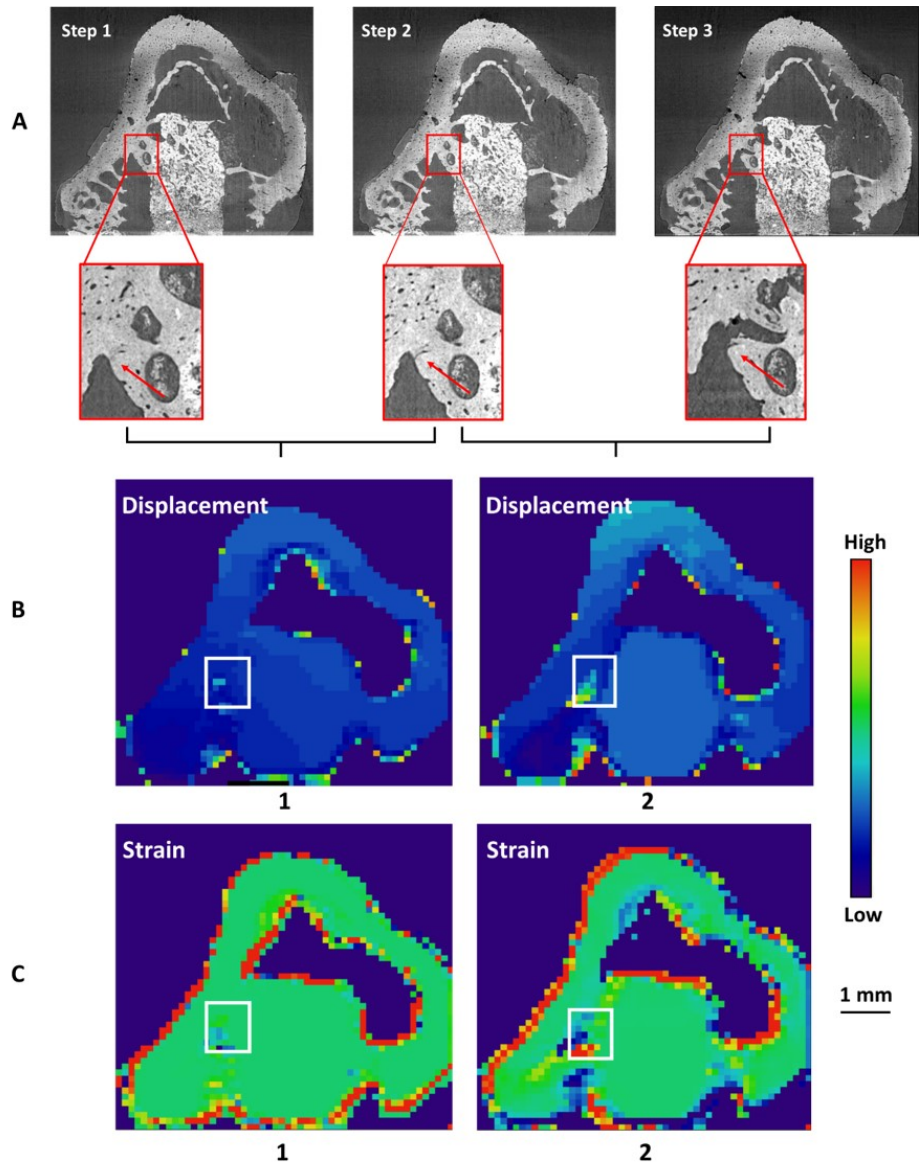

Figure 5.4: Results of the DVC analyses conducted on bin 4 CT images of the control sample for a crack larger than 10 pixels. For (B-D): the first column shows the resulting fields of the DVC analysis of steps 1-2, and the second column of steps 2-3. (A) CT images with the ROIs containing the large crack for the 3 analyzed loadsteps. (B) Displacement magnitude fields. (C) Strain fields.

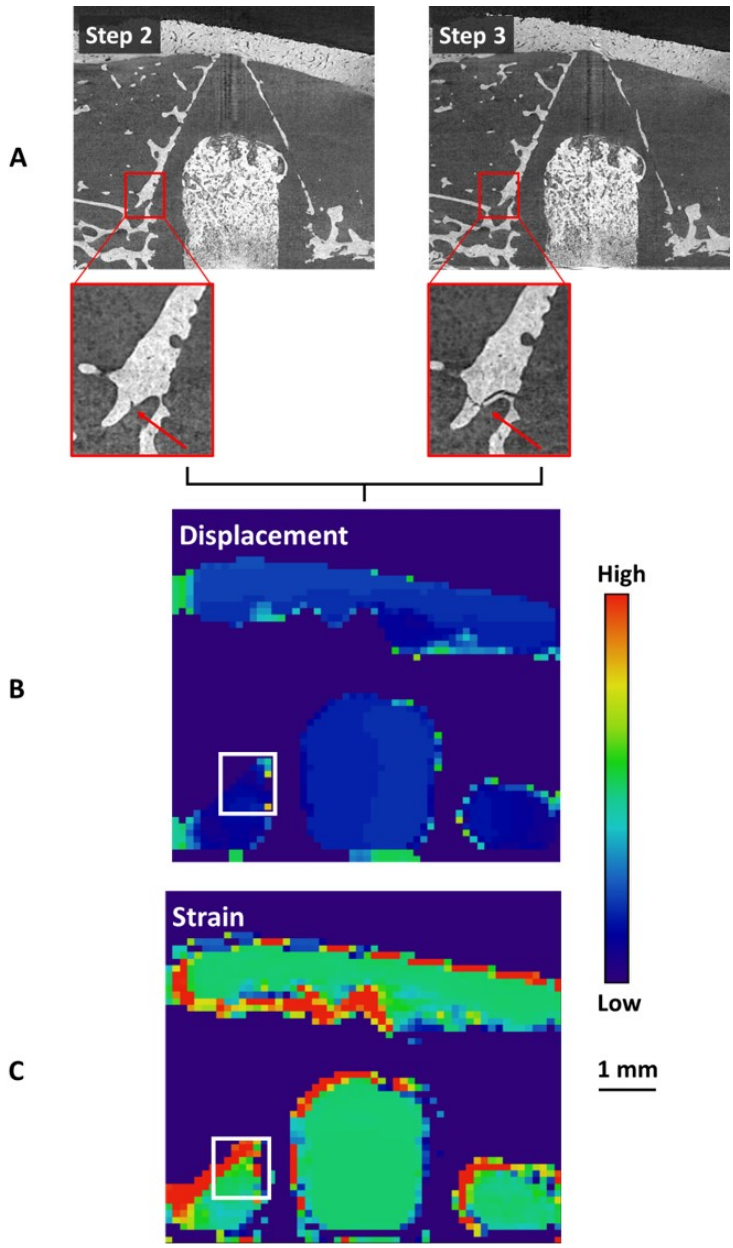

Figure 5.5: Results of the DVC analysis conducted on bin 4 CT images of the control sample for a crack smaller than 10 pixels. (A) CT images with the ROIs containing the fine crack for the final analyzed loadsteps (steps 2-3). (B) Displacement magnitude fields. (C) Strain fields.

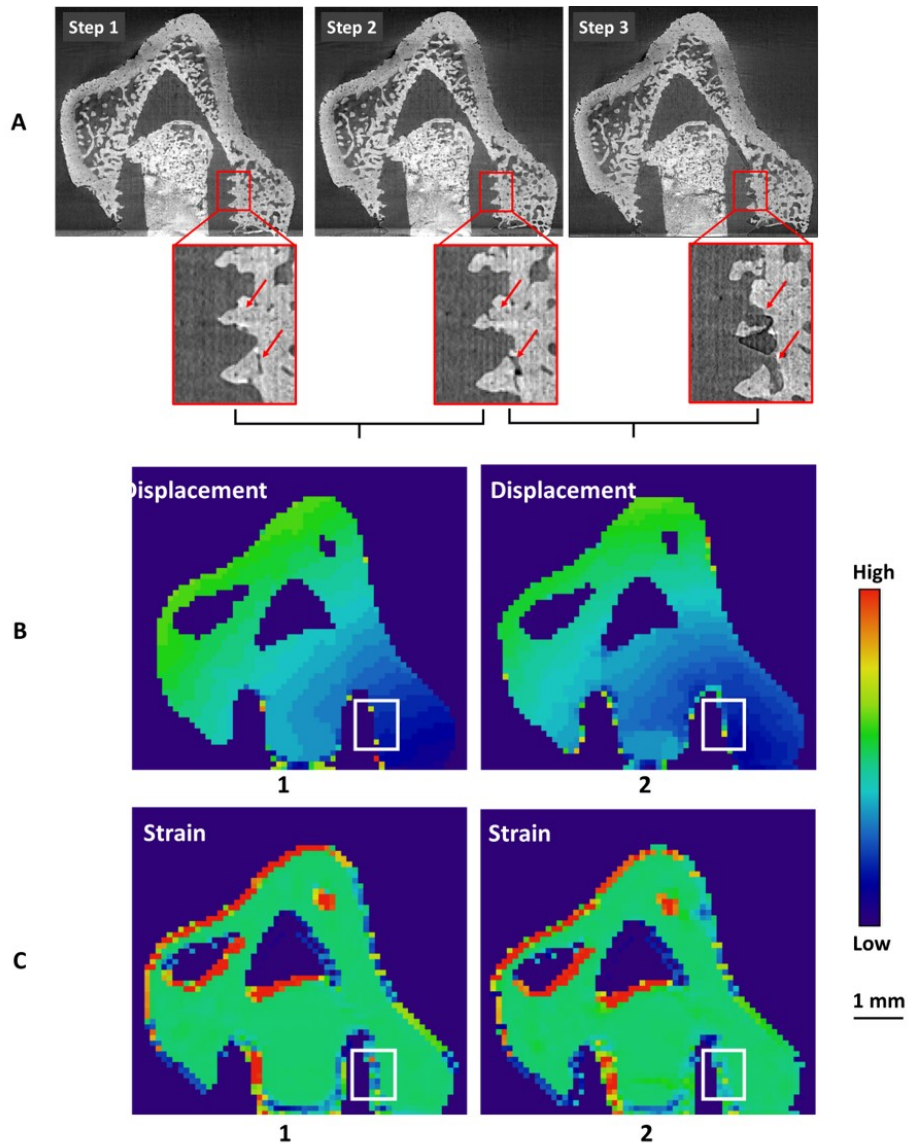

Figure 5.6: Results of the DVC analyses conducted on bin 4 CT images of the treated sample for a crack larger than 10 pixels. For (B-D): the first column shows the resulting fields of the DVC analysis of steps 1-2, and the second column of steps 2-3. (A) CT images with the ROIs containing the large crack for the 3 analyzed loadsteps. (B) Displacement magnitude fields. (C) Strain fields.

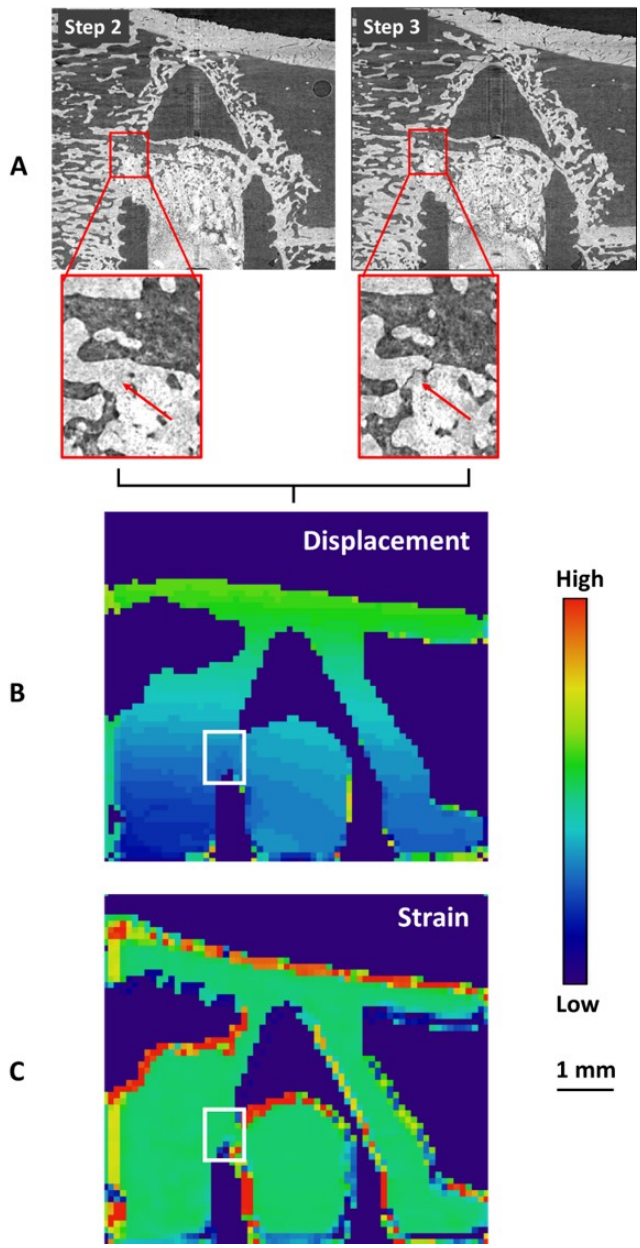

Figure 5.7: Results of the DVC analysis conducted on bin 4 CT images of the treated sample for a crack smaller than 10 pixels. (A) CT images with the ROIs containing the fine crack for the final analyzed loadsteps (steps 2-3). (B) Displacement magnitude fields. (C) Strain fields.

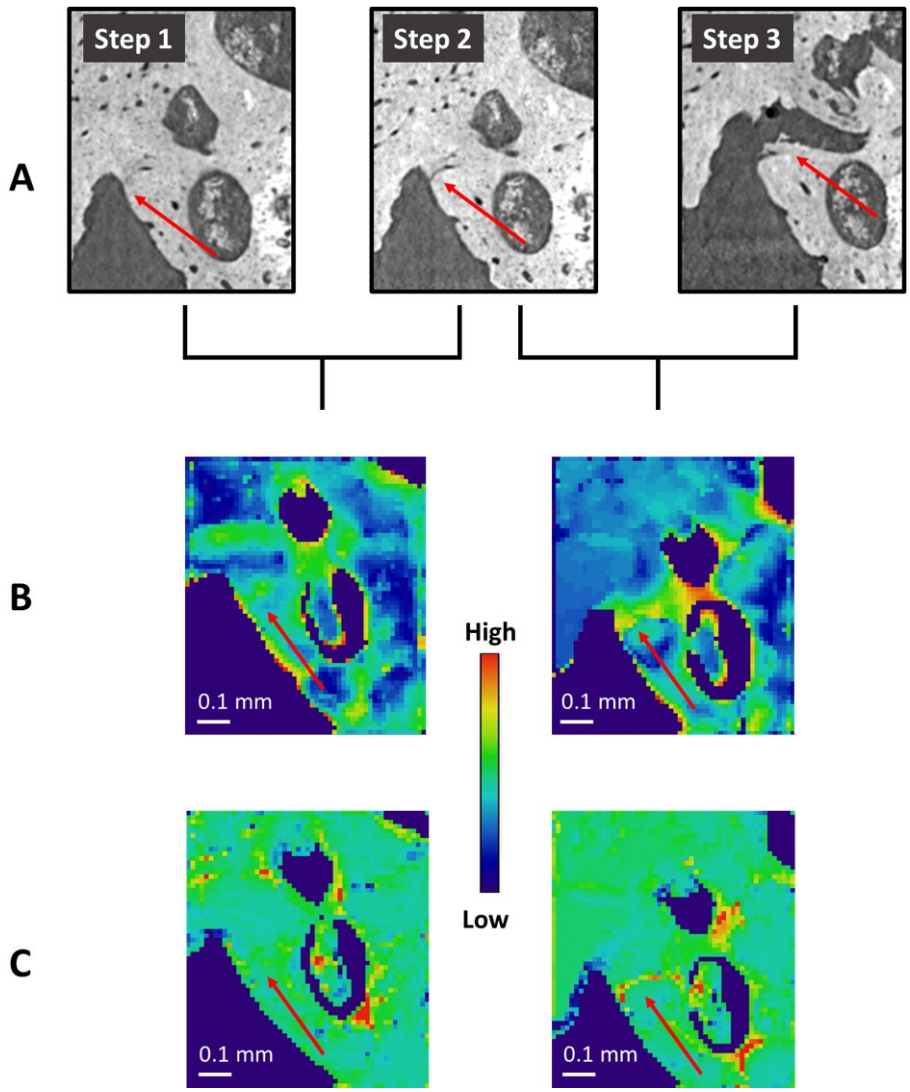

Figure 5.8: Results of the DVC analyses conducted on high-resolution CT images of the control sample. (A) Bin 1 CT images of the ROI containing the larger crack for the 3 analyzed loadsteps. Crack locations are shown with red arrows. (B) Displacement magnitudes after DVC. (C) Strains after DVC.

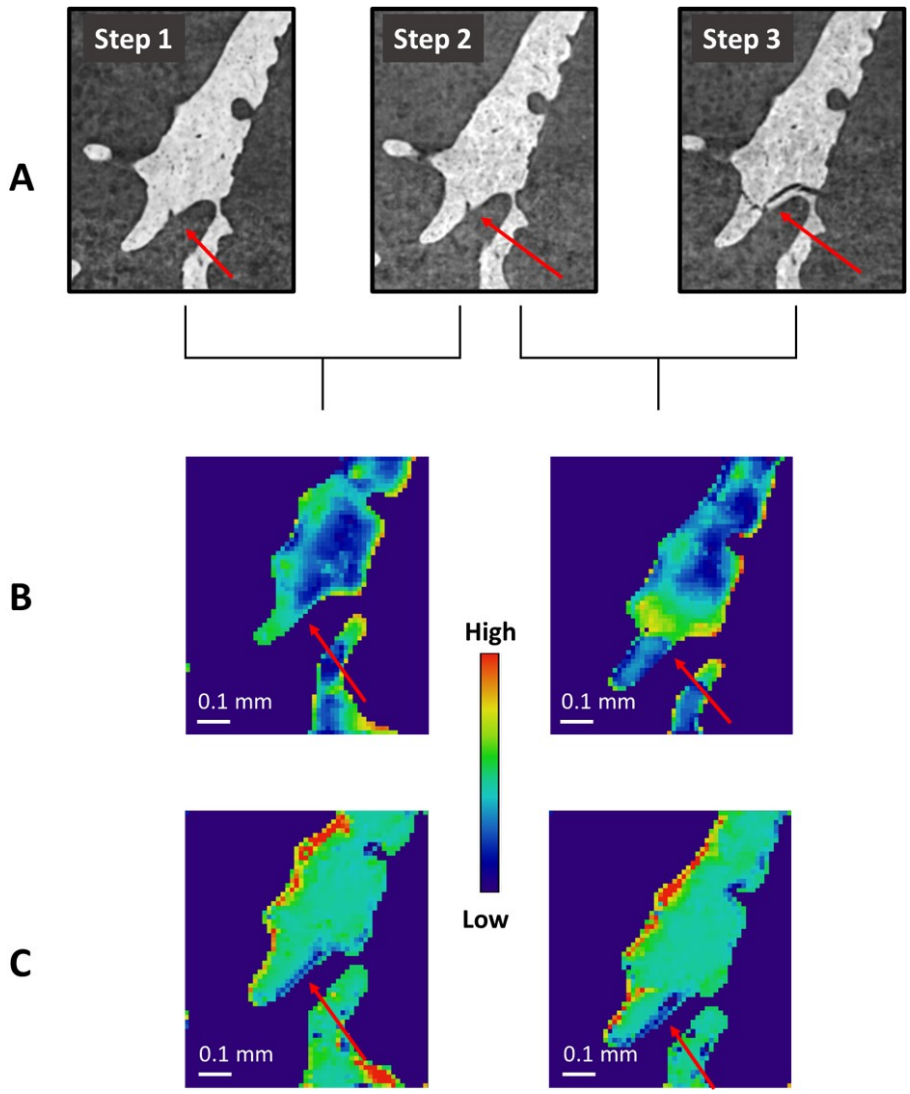

Figure 5.9: Results of the DVC analyses conducted on high-resolution CT images of the control sample. (A) Bin 1 CT images of the ROI containing the fine crack for the 3 analyzed loadsteps. Crack locations are shown with red arrows. (B) Displacement magnitudes after DVC. (C) Strains after DVC.

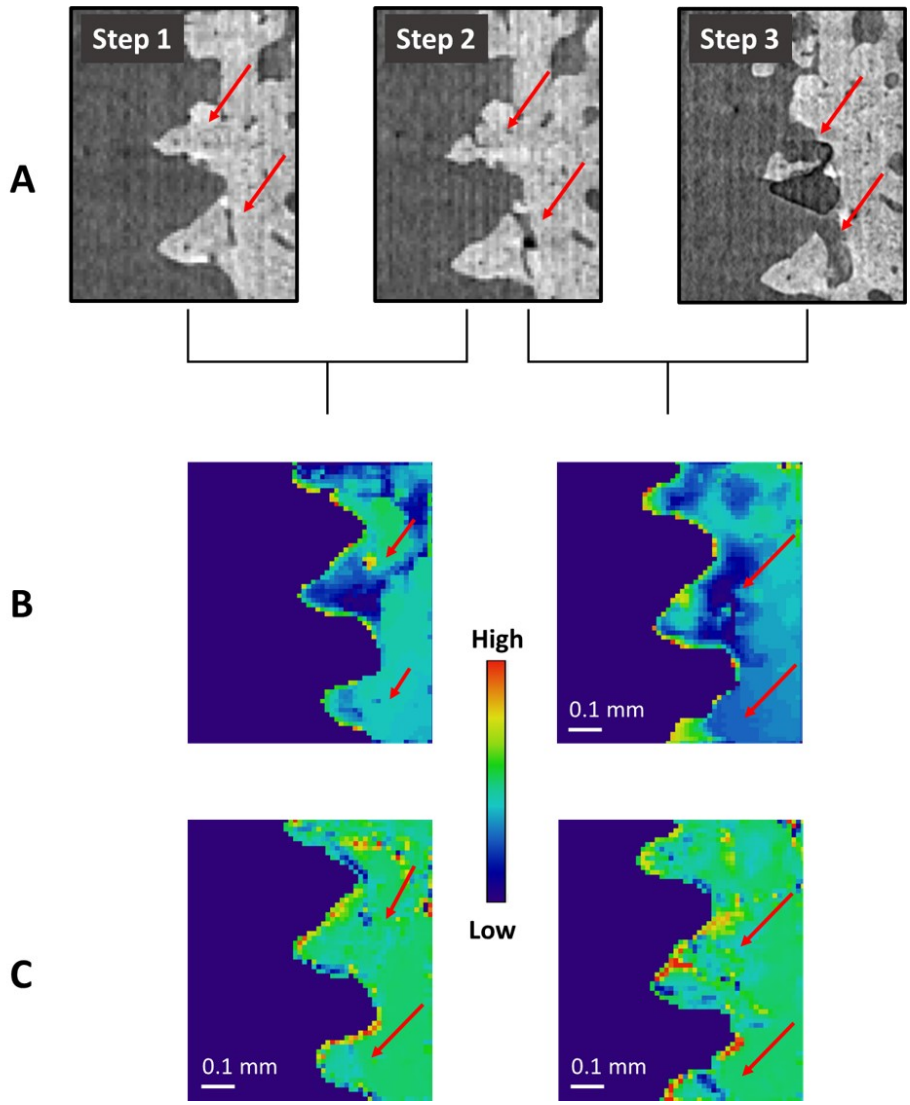

Figure 5.10: Results of the DVC analyses conducted on high-resolution CT images of the control sample. (A) Bin 1 CT images of the ROI containing the larger crack for the 3 analyzed loadsteps. Crack locations are shown with red arrows. (B) Displacement magnitudes after DVC. (C) Strains after DVC.

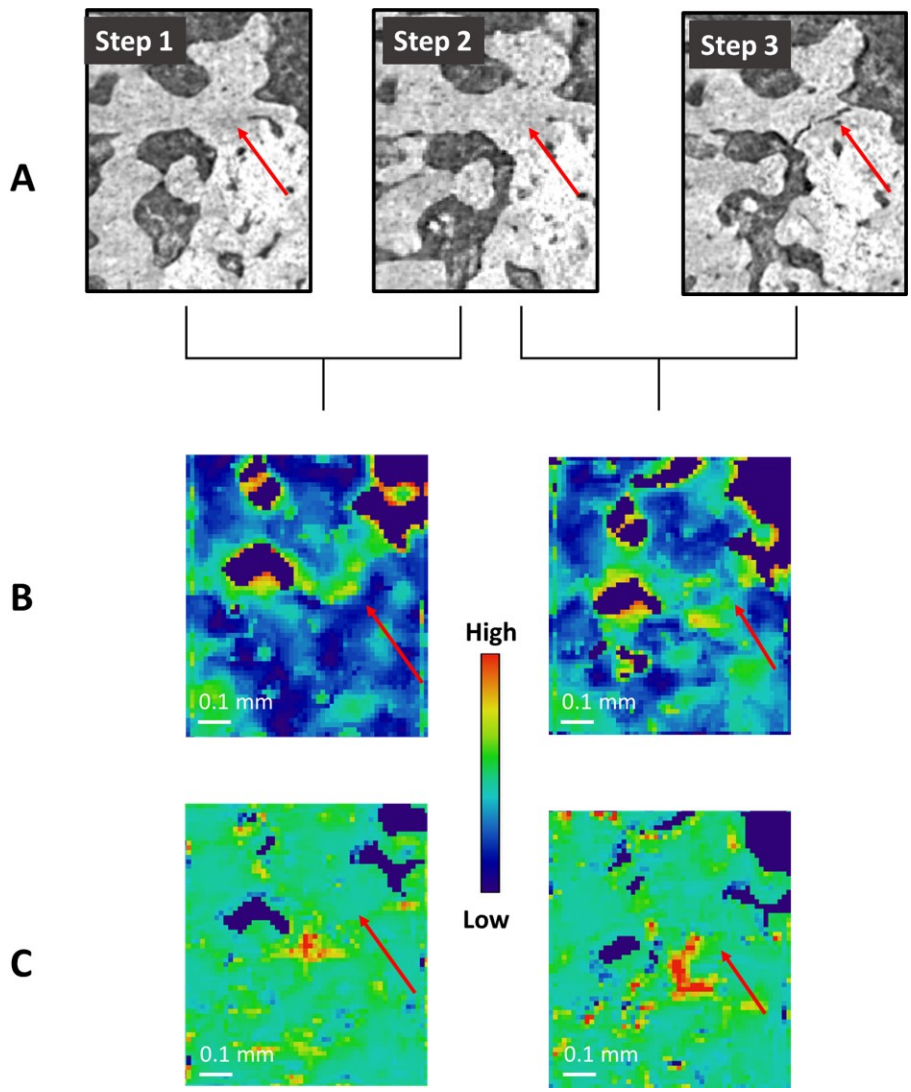

Figure 5.11: Results of the DVC analyses conducted on high-resolution CT images of the control sample. (A) Bin 1 CT images of the ROI containing the fine crack for the 3 analyzed loadsteps. Crack locations are shown with red arrows. (B) Displacement magnitudes after DVC. (C) Strains after DVC.

6 Discussion

In this section the results obtained from the various tests performed to assess the qualitative and quantitative implant integration quality, and presented in the previous section, will be discussed. A discussion of the future perspective and ethical aspect of this degree project is found at the end of this section.

6.1 *In Situ* Mechanical Testing and Imaging

Specimens were mounted on the pull-out jig to perform the pull-out tests and thereby measure their mechanical properties. Tomographic images were successfully acquired between each load-step during the pull-out tests.

During the image acquisition, the radiation dose per scan was not measured. Nevertheless, dose estimation for similar samples imaged during the same experiment indicate that the total received dose was below the limit of 35 kGy (Section 3.3.2). Furthermore, when comparing the absolute values of the mechanical properties reported by *Le Cann et al.* [7] and *Raina et al.* [6] with the values from Table 5.1, similar orders of magnitude can be noted. This enforces the belief that the results obtained in this project are reliable and that the mechanical properties were not affected by the radiation doses. Nonetheless, absolute values of the results presented in Section 5.1 cannot be interpreted with full certainty.

As was made visible by the data in Table 5.1, the mean values of peak force, peak displacement, stiffness, and fracture energy all increased for the group of implants that was treated with bioactive molecules when compared to controls. Interestingly, sample *T11* of the treated group showed low values for all mechanical properties, which were more in line with values calculated for the control group. The treatment might not have had effect on this specimen. Nevertheless, the overall increasing trend shown for all mechanical properties confirm what was reported in previous studies [6, 7], which is that local treatment with bioactive molecules such as rhBMP-2 and ZA improve the mechanical properties and that the overall variations in the mechanical behavior of the bone construct are dependent on biological factors. The supply of rhBMP-2 stimulated the differentiation of osteoblast progenitor cells into mature bone cells, thereby regenerating bone and enhancing bone formation, while the use of ZA inhibited the osteoclast inhibiting effect and reduced the bone re-

sorption [6, 7]. The higher pull-out forces needed to extract the treated implants are also an indication that the implant was better integrated with the native bone compared to the control implants.

The variability present in the mechanical data of the tested samples could stem from the use of PEEK implants instead of metal implants used in previous studies (e.g., [7]). With metal implants, a good connection could be made between the metal screw and a metal hinge used to pull the screw out of the bone. In the present study, a connection piece needed to be screwed in a plastic material, sometimes causing slippage and bad connections between the different pieces of the mechanical set-up. Therefore, the variability of the mechanical data increases. More research should be done to improve this mechanical set-up.

It is interesting to note the higher absolute values of the mechanical properties reported by *Raina et al.* [6] compared to Table 5.1. In [6], the mean peak force, fracture energy and stiffness were approximately 175N, 100 N/mm, 220 N/mm respectively for the treated group and 115N, 75 N/mm, 140 N/mm, respectively for the control group. While the mean stiffness of [6] can be considered similar to the mean stiffness of Table 5.1, the mean peak force obtained in this study was half as big as the one from [6], and the fracture energy of the control group was almost a factor 10 smaller than the one obtained in [6]. This difference most likely stems from having performed incremental pull-outs in this degree project. in contrast to continuous pull-outs. The higher displacement rate in [6] could also be a cause of these differences in values.

The pull-out tests performed for this degree project were conducted with stepwise loading of the samples. The loading was done with displacement increments of 0.15 mm as these ensured good compatibility between image acquisition speed and loading rate. Additionally, this made sure the radiation dose stayed below the 35kGy value until complete fracture of the bone. However, using incremental pull-outs resulted in load-curves that showed a force drop whenever the imaging was started for a certain load step. Continuous loading could result in better load curves, but for the image acquisition during the mechanical pull-out tests, a specimen was allowed to move no more than one pixel during each image acquisition to not induce movement artifacts in the image data. Despite the fast image acquisition (30 s/tomogram), the displacement rate needed for such small deformation would yield biologically irrelevant mechanical data, making continuous pull-out impractical for this project.

6.2 Bone Volume Analysis

A significant average increase of 250.35% in bone volume fraction around the implant resulted from treating implants with rhBMP-2 and ZA (first column in Table 5.2). This was expected based on the results of previous studies [6, 7, 9].

The study of *Le Cann et al.* [7] also showed a significant BV/TV increase when using a BMP + ZA treatment, but with maximum BV/TV reaching lower absolute values ($\approx 25\%$) in the treated group. Important to keep in mind when assessing the effect of the treatment is the different ROI definition in [7]. The trabecular ROI in [7] started 1 mm proximal to the screw edge and ended 1 mm distal to the screw edge due to significant metal artifacts close to the implant. The BV/TV results presented in 5.2 were obtained for the close implant interface since no metal artifacts prohibited this measurement.

Interestingly, sample *T11* showed a remarkably low BV/TV percentage ($\approx 16\%$) compared to the other samples of its group. The BV/TV value is more like the BV/TV values obtained in the control group. This lower bone volume fraction could explain the weaker mechanical properties of *T11* noted in Section 6.1 (Table 5.1). The weak peri-implant bone formation, combined with the weak mechanical properties of *T11* (Table 5.1), supports the findings of [10], i.e., the amount of bone material is the most important contributor to strength.

To gain further quantitative insight on the peri-implant bone formation, the correlations between BV/TV and the mechanical parameters discussed in Section 6.1 were investigated (Figure 5.3). Based on study [7], a strong positive correlation between BV/TV and stiffness was expected as well as between BV/TV and maximum force. From what can be seen in Figure 5.3, peak force and stiffness showed an insignificant amount of correlation with BV/TV ($p = 0.17$ and 0.49, respectively). Nevertheless, a positive correlation can be noted between the peak force and stiffness, and BV/TV.

The deviation of the correlations between BV/TV and the mechanical properties in [7] and this present project, could stem from the differences in study design. The main difference between both studies being the delivery mechanism of the bioactive molecules. The treatment in [7] was brought into contact with the implant surface trough injection of the bioactive molecules inside the drilled hole in the tibiae before implant insertion, while the molecules in this project were impacted inside the biomaterial

that was within the implant.

Additionally, the study of [7] differed in the following ways: the mechanical testing was conducted on bone-metal implant interfaces, the bone volume fraction was analyzed in a larger ROI around the screw and the integration time was of 4 weeks, contrarily to the PEEK implants used in this study, the close interface ROI bone fraction analysis, and the 6-week integration time. As mentioned in Section 6.1, the PEEK implant material made the mechanical testing more challenging and the mechanical data less reliable. These factors could have affected the correlations between the structural and mechanical parameters.

According to [7], differences in screw implantation, such as contact between threads and cortex as well as minor tilt of the screw also correlate with the mechanical parameters. Further investigation into these factors should be performed to better understand the obtained correlations between the mechanical parameters and BV/TV.

6.3 Digital Volume Correlation

DVC analyses were performed to gain information about the 3D displacements, and strain distributions within a control and a treated sample under loading. A deeper analysis of key high-strain regions around the implant was also conducted to investigate deformation and strain more locally. DVC served as a useful tool to identify regions where local damage occurred before total failure. When the cracking or opening of the trabecular bone at failure was bigger than 10 pixels (27.5 μm), an analysis of the bin 4 images sufficed to locate the high displacements, and consequently, the high-strain regions. If smaller cracking needed to be detected, higher resolution images were needed.

The uncertainties in the DVC measurements for the bin 1 and bin 4 analyses were higher than the accuracy and precision values presented in [87] and [9], for the displacement and strain components, respectively. The high strain errors make the quantitative values of the computed strains by the DVC unreliable. Therefore, DVC strain fields were only used for the qualitative analysis of crack formation and location. In [9], the highest percentage error for the displacements was of 0.014%, which is approximately 2 orders of magnitude smaller than the percentage errors displayed in Table 5.4. Even though the displacement percentage errors were all below 5%, the displacement magnitude fields were also only used for a

qualitative assessment of the displacements.

The analysis of crack locations and initiation was conducted solely based on the displacement magnitude fields for a couple of reasons. Firstly, as the strain fields were calculated based on the displacement fields, additional errors could have been induced during the strain computation. Steep gradients of displacement are reliable enough as these consequently result in high strains. Secondly, as some cracks were already observed during the first analyzed loadstep of both samples, the resulting strain values of the DVC analyses were unrealistic. Reducing the size of the loadsteps could help detect high-strain regions where damage has not yet occurred. Finally, the trabecular bone analyzed with DVC is composed of thin structures. These thin structures are hard to detect with DVC and usually result in erroneous high values of strain at the thin edges of the bone structures. As most cracks appear close to edges, smaller cracks could not be identified using lower resolution images or with coarse DVC input parameters, i.e., bigger node spacing and smaller correlation windows. By using higher-resolution images, the resolution of the resulting DVC fields increased, making the unreliable high-strain edges less relevant.

The analysis of the control and treated sample suggest that steep displacement gradients mainly occurred at the level of the threads of the implant, and at the newly formed trabecular bone around the implant.

For the treated sample, the steep displacement gradients matched with the regions visually identified in the μCT scans. The data from this sample showed that the high displacement locations derived from the DVC analyses are good indicators of cracks and zones where implant failure and bone fracture will occur before total failure. Eventually, DVC was able to detect clear changes in displacement magnitudes in bone regions where small cracking was initially not visually identified in the μCT images.

Nevertheless, within the treated sample, DVC had some more trouble detecting the cracks. The big crack (See Figure 4.12) was only well detected when using high resolution images. The finer crack was harder to notice in the displacement fields of the final loadsteps since a lot of deformation was happening in its surrounding bone region. The detection difficulty could also stem for the mask used to remove the void and background pixels, which did not mask away all void pixels in that ROI. The size of the analyzed cracks could also have influenced the DVC ability to find a

proper match within the set CW. Further investigation of different sizes of cracks, in different ROI could be conducted to tailor DVC's use.

Overall, DVC can be a useful tool to identify regions in early loadsteps where local damage may occur when additional loading is applied. It can also be concluded that the surrounding bone region of a crack, the image resolution and cracks size all had an influence on the crack detection. DVC can be used to detect big cracks based on lower resolution bin 4 images when a neat crack occurs in an environment with less bone density. For a crack occurring in a region with high bone density and high deformation, DVC will have a harder time detecting specific cracks. In that case, high-resolution images should be used and more precise void and background pixel masking is recommended.

6.4 Future Perspective

The obtained results of this Master's thesis project could be further improved by integrating some new aspects. The results could also be useful for human applications in the orthopedic field.

Firstly, the PEEK implants used in this degree project prevented the occurrence of metal imaging artifacts, which was a recurring limitation in previous studies. Nevertheless, ring artifacts and dark shadowing present in the CT images of some loaded samples prevented the proper masking of void and background, which complicated the DVC analysis. In future studies, focus should be on reducing these artifacts.

Secondly, this project led to useful insight about the structural and mechanical properties of peri-implant bone by studying the bone formation and mechanical parameters of the newly formed bone. Previous studies reported that the screw insertion parameters: screw tilt, screw contact surface with the cortex and distance between the screw and tibial plateau; had an influence on the mechanical stability of implants [6]. This aspect of mechanical stability was not investigated here, but it could certainly be an interesting addition to this project.

Thirdly, DVC has shown to be able to detect fractures, but the quality of the detection is dependent of the type of fracture. If given more time, more focus could have been given to the development of better masking of void and background pixels, especially in dense bone regions with small voids. Eventually, this tool could be used in diverse studies where mechanical behaviour and fracture behaviour are investigated.

Finally, the addition of the bioactive molecules rhBMP-2 and ZA to the CaS/HA biomaterial inside the implant caused improvements in structural and mechanical properties. This led to an improvement of the stability of the implants in the bone and the quality of the regenerated bone around the implant. By conducting clinical trials and using these bioactive molecules in a clinical treatment, an improvement in bone fracture healing could be possible for human bones as well. In order to achieve this goal of human applications, more experimental trials could be carried out on higher mammals. Minipigs or sheep for example, have shown a metabolic bone rate that is more comparable to that of humans [88, 89]. By supporting the results of the present study with further experiments, the conclusions drawn from this study could be extrapolated to human orthopedic applications. The improved bone-implant integration and mechanical characteristics of the bone would contribute to an improved quality of life of patients as the need for revision surgery in orthopedics and the occurrence of implant loosening would be reduced.

6.5 Ethical Reflection

The animal model with the tibia defect model used to bring the implants into the rat tibiae, was ethically approved for use by the Swedish board of agriculture and the regional animal research ethics committee (Permit number: M79-15 and 15288/2019). Institutional guidelines for the care and treatment of experimental animals were followed. The rats had free access to food pellets and water throughout the 6-week duration of the implant integration. Animals were housed two/cage with 12 h light/darkness cycles. The biomaterial (Cerament) and bioactive molecules (rhBMP-2 and ZA) used in this experiment were all approved for clinical use.

As pull-out tests were performed to gain insight on the structure of peri-implant bone under loading, an alternative to animal testing was not available. Re-using collected data from similar previous studies was also not an option, as that data had already been analyzed and the studies were published. However, the sample size of this study (N = 21) was reduced to a minimum, while still including enough specimens to account for biological variation and to allow for significant biological conclusions.

The results from this research enabled to gain a deeper understanding of how and to what extend drug treatments can influence the quality of bone-implant integration. The conclusions drawn from this study serve as a solid base for possible extrapolation of the results to human ortho-

pedic applications and further studies about alternative drug treatments and imaging for implants. Improved bone-implant integration would contribute to an improved quality of life of patients as the need for revision surgery in orthopedics and the occurrence of implant loosening would be reduced.

Most information presented in this degree project has been obtained from peer-reviewed journal publications and was critically reviewed. Multiple sources were consulted to ensure the veracity of each reported material. Figures taken from publications were either altered or redrawn.

7 Conclusion

The parameter BV/TV showed significant correlations with peak displacement and fracture energy. The results from the quantitative mechanical analysis and bone volume analysis suggest that the mechanical and structural properties increased for the PEEK implants filled with the CaS/HA carrier and rhBMP-2 + ZA bioactive molecules, thereby enhancing the bone-implant stability.

Furthermore, DVC was an efficient tool to identify bone fracturing before total implant failure in terms of locations for both the treated and untreated sample. When wanting to detect finer cracks (i.e., < 10 pixels) in trabecular bone, high-resolution images are needed. For bigger cracks, lower resolution images such as bin 4 images, could suffice to detect high-strain regions.

Cracks were observed in both control and treated cases, but since the treated samples had higher BV/TV, the fracture loads were higher. DVC showed that cracks approximately appeared in the same locations for treated and control samples, i.e., at the treads and the thin newly generated peri-implant bone, and the difference is mostly observed in BV/TV. The BV/TV is a key factor in determining the pull-out strength.

Translating these observations to human orthopedic applications will help improve peri-implant bone quantity and quality. This could lead to a reduced number of reoperations, thereby increasing the quality of life of patients and decreasing the financial burden of undergoing orthopedic surgery.

References

[1] S. Rajendran, S. C. Anand, and A. J. Rigby, "5 - Textiles for healthcare and medical applications," in *Handbook of Technical Textiles (Second Edition)*, A. R. Horrocks and S. C. Anand, Eds. Woodhead Publishing, 2016, pp. 135–168.

[2] W. Jin and P. K. Chu, "Orthopedic Implants," in *Encyclopedia of Biomedical Engineering*, R. Narayan, Ed. Elsevier, 2019, pp. 425–439.

[3] J. Kärrholm, C. Rogmark, E. Naucler, J. Nåtman, J. Vinblad, M. Mohaddes, and O. Rolfson, *Swedish Hip Arthroplasty Register: Annual Report 2019*. Swedish Hip Arthroplasty Register, 2021.

[4] S. Landgraeber, M. Jäger, J. J. Jacobs, and N. J. Hallab, "The Pathology of Orthopedic Implant Failure Is Mediated by Innate Immune System Cytokines," *Mediators of Inflammation*, vol. 2014, p. e185150, 2014.

[5] P. H. Wooley and E. M. Schwarz, "Aseptic loosening," *Gene Therapy*, vol. 11, no. 4, pp. 402–407, 2004.

[6] D. B. Raina, D. Larsson, E. A. Sezgin, H. Isaksson, M. Tägil, and L. Lidgren, "Biomodulation of an implant for enhanced bone-implant anchorage," *Acta Biomaterialia*, vol. 96, pp. 619–630, 2019.

[7] S. Le Cann, E. Tudisco, M. J. Turunen, A. Patera, R. Mokso, M. Tägil, O. Belfrage, S. A. Hall, and H. Isaksson, "Investigating the Mechanical Characteristics of Bone-Metal Implant Interface Using in situ Synchrotron Tomographic Imaging," *Frontiers in Bioengineering and Biotechnology*, vol. 6, 2019.

[8] S. Le Cann, E. Tudisco, M. Tägil, S. A. Hall, and H. Isaksson, "Bone Damage Evolution Around Integrated Metal Screws Using X-Ray Tomography — in situ Pullout and Digital Volume Correlation," *Frontiers in Bioengineering and Biotechnology*, vol. 8, 2020.

[9] S. Le Cann, E. Tudisco, C. Perdikouri, O. Belfrage, A. Kaestner, S. Hall, M. Tägil, and H. Isaksson, "Characterization of the bone-metal implant interface by digital volume correlation of in-situ loading using neutron tomography," *Journal of the Mechanical Behavior of Biomedical Materials*, vol. 75, pp. 271–278, 2017.

[10] M. J. Turunen, S. Le Cann, E. Tudisco, G. Lovric, A. Patera, S. A. Hall, and H. Isaksson, "Sub-trabecular strain evolution in human trabecular bone," *Scientific Reports*, vol. 10, no. 1, p. 13788, 2020.

[11] J. Buckwalter and R. Cooper, "Bone structure and function." *Instructional Course Lectures*, vol. 36, pp. 27–48, 1987.

[12] B. Clarke, "Normal bone anatomy and physiology," *Clinical Journal of the American Society of Nephrology*, vol. 3, no. Supplement 3, pp. S131–S139, 2008.

[13] N. Swailes, "1.7.2 Types of Bone," Available: https://nathan-swailes.squarespace.com/172-typesofbone, Hawkeye Histology, [Online; Visited on: 2021-05-27].

[14] F. H. Martini, J. L. Nath, and E. F. Bartholomew, "Chapter 6 - bones and bone structure," in *Fundamentals of Anatomy & Physiology*, 11th ed. Pearson, 2018, pp. 226–253.

[15] Anon., "DoITPoMS - TLP library structure of bone and implant materials - structure and composition of bone," Available: https://www.doitpoms.ac.uk/tlplib/bones/structure.php, University of Cambridge, [Online; Visited on: 2021-05-15].

[16] M. Mehta, K. Schmidt-Bleek, G. N. Duda, and D. J. Mooney, "Biomaterial delivery of morphogens to mimic the natural healing cascade in bone," *Advanced Drug Delivery Reviews*, vol. 64, no. 12, pp. 1257–1276, 2012.

[17] T. Kim, C. W. See, X. Li, and D. Zhu, "Orthopedic implants and devices for bone fractures and defects: Past, present and perspective," *Engineered Regeneration*, vol. 1, pp. 6–18, 2020.

[18] P. V. Giannoudis, T. A. Einhorn, and D. Marsh, "Fracture healing: The diamond concept," *Injury*, vol. 38, pp. S3–S6, 2007.

[19] R. Marsell and T. A. Einhorn, "The biology of fracture healing," *Injury*, vol. 42, no. 6, pp. 551–555, 2011.

[20] S. Dogramadzi, D. Raabe, and R. Atkins, "A system for anatomical reduction of bone fractures," 2011, US Patent App. 14/343,583.

[21] Miller-Keane Encyclopedia and Dictionary of Medicine, Nursing, and Allied Health, "Callus - The Free Dictionary," Available: https://medical-dictionary.thefreedictionary.com/callus, 2003, [Online; Visited on: 2021-05-27].

[22] M. S. Ghiasi, J. Chen, A. Vaziri, E. K. Rodriguez, and A. Nazarian, "Bone fracture healing in mechanobiological modeling: A review of principles and methods," *Bone Reports*, vol. 6, pp. 87–100, 2017.

[23] A. R. Shrivats, P. Alvarez, L. Schutte, and J. O. Hollinger, "Chapter 55 - Bone Regeneration," in *Principles of Tissue Engineering (Fourth Edition)*, R. Lanza, R. Langer, and J. Vacanti, Eds. Academic Press, 2014, pp. 1201–1221.

[24] H. A. Wallace, B. M. Basehore, and P. M. Zito, "Wound healing phases," *StatPearls*, 2017.

[25] J. R. Sheen and V. V. Garla, "Fracture healing overview," *StatPearls*, 2020.

[26] P. Pivonka and C. R. Dunstan, "Role of mathematical modeling in bone fracture healing," *BoneKEy reports*, vol. 1, 2012.

[27] P. R. Kuzyk and E. H. Schemitsch, "The basic science of peri-implant bone healing," *Indian Journal of Orthopaedics*, vol. 45, no. 2, pp. 108–115, 2011.

[28] Y. Manor, S. Oubaid, O. Mardinger, G. Chaushu, and J. Nissan, "Characteristics of early versus late implant failure: a retrospective study," *Journal of Oral and Maxillofacial Surgery*, vol. 67, no. 12, pp. 2649–2652, 2009.

[29] V. H. Kastala, "Methods to measure implant stability," *Journal of Dental Implants*, vol. 8, no. 1, p. 3, 2018.

[30] A. Hudecki, G. Kiryczyński, and M. J. Łos, "Chapter 7 - biomaterials, definition, overview," in *Stem Cells and Biomaterials for Regenerative Medicine*, M. J. Łos, A. Hudecki, and E. Wiecheć, Eds. Academic Press, 2019, pp. 85–98.

[31] D. Pioletti, "16 - Using drug delivery systems to enhance joint replacement," in *Joint Replacement Technology*, ser. Woodhead Publishing Series in Biomaterials, P. A. Revell, Ed. Woodhead Publishing, 2008, pp. 397–406.

[32] R. Karuppal, "Biological fixation of total hip arthroplasty: Facts and factors," *Journal of Orthopaedics*, vol. 13, no. 3, pp. 190–192, 2016.

[33] M. GINEBRA, "10 - cements as bone repair materials," in *Bone Repair Biomaterials*, ser. Woodhead Publishing Series in Biomaterials, J. A. Planell, S. M. Best, D. Lacroix, and A. Merolli, Eds. Woodhead Publishing, 2009, pp. 271–308.

[34] BONESUPPORT, "CERAMENT® BONE VOID FILLER," Available: https://bonesupport.com/en-eu/products/cerament-bone-void-filler/, BONESUPPORT, [Online; Visited on: 2021-05-29].

[35] Z. Li, G. Kuhn, M. von Salis-Soglio, S. J. Cooke, M. Schirmer, R. Müller, and D. Ruffoni, "In vivo monitoring of bone architecture and remodeling after implant insertion: The different responses of cortical and trabecular bone," *Bone*, vol. 81, pp. 468–477, 2015.

[36] J. Odekerken, T. Welting, J. Arts, G. Walenkamp, and P. Emans, "Modern Orthopaedic Implant Coatings — Their Pro's, Con's and Evaluation Methods," in *Modern Surface Engineering Treatments*, 2013.

[37] J. Orth, S. Macedo, A. Wilke, and P. Griss, "Osseointegration of Hydroxyapatite-Coated and Uncoated Bulk Alumina Implants in the Femur of Göttingen Minipigs Mechanical Testing of Bonding Strength," in *Bioceramics and the Human Body*, A. Ravaglioli and A. Krajewski, Eds. Springer Netherlands, 1992, pp. 302–307.

[38] S.-W. Lee, B.-D. Hahn, T. Y. Kang, M.-J. Lee, J.-Y. Choi, M.-K. Kim, and S.-G. Kim, "Hydroxyapatite and Collagen Combination-Coated Dental Implants Display Better Bone Formation in the Peri-Implant Area Than the Same Combination Plus Bone Morphogenetic Protein-2–Coated Implants, Hydroxyapatite Only Coated Implants, and Uncoated Implants," *Journal of Oral and Maxillofacial Surgery*, vol. 72, no. 1, pp. 53–60, 2014.

[39] J. Li, G. Yang, T. Siebert, M. F. Shi, and L. Yang, "A method of the direct measurement of the true stress–strain curve over a large strain range using multi-camera digital image correlation," *Optics and Lasers in Engineering*, vol. 107, pp. 194–201, 2018.

[40] H. Kanno, T. Aizawa, K. Hashimoto, and E. Itoi, "Enhancing percutaneous pedicle screw fixation with hydroxyapatite granules: A biomechanical study using an osteoporotic bone model," *PLOS ONE*, vol. 14, p. e0223106, 2019.

[41] R. Zdero, M. S. R. Aziz, and B. Nicayenzi, "Chapter 8 - Pullout Force Testing of Cortical and Cancellous Screws in Whole Bone," in *Experimental Methods in Orthopaedic Biomechanics*, R. Zdero, Ed. Academic Press, 2017, pp. 117–132.

[42] C. H. Turner, "Bone strength: Current concepts," *Annals of the New York Academy of Sciences*, vol. 1068, pp. 429–446, 2006.

[43] S. Tavana, J. N Clark, N. Newell, J. D. Calder, and U. Hansen, "In vivo deformation and strain measurements in human bone using digital volume correlation (dvc) and 3t clinical mri," *Materials*, vol. 13, no. 23, p. 5354, 2020.

[44] N. Sasaki and S. Odajima, "Stress-strain curve and young's modulus of a collagen molecule as determined by the X-ray diffraction technique," *Journal of Biomechanics*, vol. 29, no. 5, pp. 655–658, 1996.

[45] A. Sharir, M. Barak, and R. Shahar, "Whole bone mechanics and mechanical testing," *Veterinary journal (London, England : 1997)*, vol. 177, pp. 8–17, 2008.

[46] H. Wang and Q.-H. Qin, "Chapter 2 - mechanics of solids and structures," in *Methods of Fundamental Solutions in Solid Mechanics*, H. Wang and Q.-H. Qin, Eds. Elsevier, 2019, pp. 53–90.

[47] MedecineNet, "Definition of Tomography," Available: https://www.medicinenet.com/tomography/definition.htm, MedicineNet, [Online; Visited on: 2021-05-22].

[48] H. Hiriyannaiah, "X-ray computed tomography for medical imaging," *IEEE Signal Processing Magazine*, vol. 14, no. 2, pp. 42–59, 1997.

[49] T. M. Buzug, "Computed Tomography," in *Springer Handbook of Medical Technology*, ser. Springer Handbooks, R. Kramme, K.-P. Hoffmann, and R. S. Pozos, Eds. Springer, 2011, pp. 311–342.

[50] M. Chappell, "Transmission—X-rays," in *Principles of Medical Imaging for Engineers: From Signals to Images*, M. Chappell, Ed. Springer International Publishing, 2019, pp. 9–18.

[51] F. H. Martini, J. L. Nath, and E. F. Bartholomew, "Chapter 1 - An Introduction to Anatomy and Physiology," in *Fundamentals of Anatomy & Physiology*, 11th ed. Pearson, 2018, pp. 47–72.

[52] M. H. McKetty, "The AAPM/RSNA physics tutorial for residents. X-ray attenuation." *RadioGraphics*, vol. 18, no. 1, pp. 151–163, 1998.

[53] T. E. Gureyev, S. C. Mayo, D. E. Myers, Y. Nesterets, D. M. Paganin, A. Pogany, A. W. Stevenson, and S. W. Wilkins, "Refracting Röntgen's rays: Propagation-based x-ray phase contrast for biomedical imaging," *Journal of Applied Physics*, vol. 105, no. 10, p. 102005, 2009.

[54] M. Endrizzi, "X-ray phase-contrast imaging," *Nuclear Instruments and Methods in Physics Research Section A: Accelerators, Spectrometers, Detectors and Associated Equipment*, vol. 878, pp. 88–98, 2018.

[55] S.-A. Zhou and A. Brahme, "Development of phase-contrast x-ray imaging techniques and potential medical applications," *Physica Medica*, vol. 24, no. 3, pp. 129–148, 2008.

[56] S. Cheriyedath, "Micro-CT Principles, Strengths, and Weaknesses," Available: https://www.news-medical.net/life-sciences/Micro-CT-Principles-Strengths-and-Weaknesses.aspx, 2019, [Online; Visited on: 2021-06-11].

[57] E. Lin and A. Alessio, "What are the basic concepts of temporal, contrast, and spatial resolution in cardiac CT?" *Journal of cardiovascular computed tomography*, vol. 3, no. 6, pp. 403–408, 2009.

[58] Anon., "Resolution and size limitations," https://www.ctlab.geo.utexas.edu/about-ct/resolution-and-size-limitations/, The University of Texas High-Resolution X-ray Computed Tomography Facility , [Online; Visited on: 2021-06-09].

[59] L. Heuser, "Digital Radiography," in *Springer Handbook of Medical Technology*, ser. Springer Handbooks, R. Kramme, K.-P. Hoffmann, and R. S. Pozos, Eds. Springer, 2011, pp. 291–310.

[60] M. Gaurang, O. Shetty, S. Shreya, and R. D. Singh, "Measuring implant stability: A review of different methods," *Journal of Dental Implants*, vol. 4, no. 2, pp. 165–169, 2014.

[61] M. Atsumi, S.-H. Park, and H. Wang, "Methods used to assess implant stability: Current status." *undefined*, 2007.

[62] A. Du Plessis, C. Broeckhoven, A. Guelpa, and S. G. Le Roux, "Laboratory x-ray micro-computed tomography: a user guideline for biological samples," *GigaScience*, vol. 6, no. 6, p. gix027, 2017.

[63] O. P. Wennberg and L. Rennan, "A brief introduction to the use of X-ray computed tomography (CT) for analysis of natural deformation structures in reservoir rocks," *Geological Society, London, Special Publications*, vol. 459, no. 1, pp. 101–120, 2018.

[64] A. Bagnell, "What is Micro-CT? An Introduction," Available: https://www.microphotonics.com/what-is-micro-ct-an-introduction/, Micro Photonics, [Online; Visited on: 2021-05-24].

[65] J. Kastner, B. Harrer, G. Requena, and O. Brunke, "A comparative study of high resolution cone beam X-ray tomography and synchrotron tomography applied to Fe- and Al-alloys," *NDT & E International*, vol. 43, no. 7, pp. 599–605, 2010.

[66] A. Bharti and N. Goyal, *Fundamental of Synchrotron Radiations*. IntechOpen, 2019.

[67] Anon., "Production of X-Rays - FRCR Physics Notes," Available: https://sites.google.com/site/frcrphysicsnotes/production-of-x-rays, [Online; Visited on: 2021-05-24].

[68] ESRF, "What is a synchrotron?" Available: https://www.esrf.fr/about/synchrotron-science/synchrotron, European Synchrotron Radiation Facility - The European Synchrotron, [Online; Visited on: 2021-05-24].

[69] Ulflund, Available: https://commons.wikimedia.org/wiki/File:X-ray_applications.svg, 2012, [Online; Visited on: 2021-06-10].

[70] H. D. Barth, E. A. Zimmermann, E. Schaible, S. Y. Tang, T. Alliston, and R. O. Ritchie, "Characterization of the effects of x-ray irradiation on the hierarchical structure and mechanical properties of human cortical bone," *Biomaterials*, vol. 32, no. 34, pp. 8892–8904, 2011.

[71] J. F. Barrett and N. Keat, "Artifacts in CT: Recognition and Avoidance," *RadioGraphics*, vol. 24, no. 6, pp. 1679–1691, 2004.

[72] P. Corcoran and P. Bigioi, "Consumer imaging i: Processing pipeline, focus, and exposure," in *Handbook of Visual Display Technology*, J. Chen, W. Cranton, and M. Fihn, Eds. Cham: Springer International Publishing, 2016, pp. 513–544.

[73] V. Van Nieuwenhove, J. De Beenhouwer, F. De Carlo, L. Mancini, F. Marone, and J. Sijbers, "Dynamic intensity normalization using eigen flat fields in X-ray imaging," *Optics Express*, vol. 23, no. 21, pp. 27 975–27 989, 2015.

[74] P. Merken and R. Vandersmissen, "Dark current and influence of target emissivity," *Photonics Imaging Technol.*, pp. 4–6, 2016.

[75] B. Pan and B. Wang, "Some recent advances in digital volume correlation," *Optics and Lasers in Engineering*, vol. 135, p. 106189, 2020.

[76] E. Tudisco, E. Andò, R. Cailletaud, and S. A. Hall, "TomoWarp2: A local digital volume correlation code," *SoftwareX*, vol. 6, pp. 267–270, 2017.

[77] B. K. Bay, T. S. Smith, D. P. Fyhrie, and M. Saad, "Digital volume correlation: Three-dimensional strain mapping using X-ray tomography," *Experimental Mechanics*, vol. 39, no. 3, pp. 217–226, 1999.

[78] S. A. Hall, "Digital image correlation in experimental geomechanics," *ALERT Geomaterials Doctoral Summer School*, vol. 2012, pp. 69–102, 2012.

[79] B. Wang and B. Pan, "Incremental digital volume correlation method with nearest subvolume offset: An accurate and simple approach for large deformation measurement," *Advances in Engineering Software*, vol. 116, pp. 80–88, 2018.

[80] P. Linderbäck, F. Agholme, K. Wermelin, T. Närhi, P. Tengvall, and P. Aspenberg, "Weak effect of strontium on early implant fixation in rat tibia," *Bone*, vol. 50, no. 1, pp. 350–356, 2012.

[81] S. Verma, N. Sharma, S. Kango, and S. Sharma, "Developments of PEEK (Polyetheretherketone) as a biomedical material: A focused review," *European Polymer Journal*, vol. 147, p. 110295, 2021.

[82] J. Toth, "Biocompatibility of Polyaryletheretherketone Polymers," in *PEEK Biomaterials Handbook*, 2012, pp. 81–92.

[83] L. Wancket, "Animal models for evaluation of bone implants and devices: Comparative bone structure and common model uses," *Veterinary pathology*, vol. 52, 2015.

[84] Paul Scherrer Institut, "Swiss Light Source - SLS," Available: https://www.psi.ch/en/sls, [Online; Visited on: 2021-05-30].

[85] MathWorks, "2-D Gaussian filtering of images - MATLAB imgaussfilt - MathWorks Nordic," Available: https://se.mathworks.com/help/images/ref/imgaussfilt.html, [Online; Visited on: 2021-05-30].

[86] ImageJ, "ImageJ - Welcome," Available: https://imagej.net/Welcome, [Online; Visited on: 2021-05-30].

[87] L. Liu and E. F. Morgan, "Accuracy and precision of digital volume correlation in quantifying displacements and strains in trabecular bone," *Journal of biomechanics*, vol. 40, no. 15, pp. 3516–3520, 2007.

[88] E. Nkenke, F. Kloss, J. Wiltfang, S. Schultze-Mosgau, M. Radespiel-Tröger, K. Loos, and F. W. Neukam, "Histomorphometric and fluorescence microscopic analysis of bone remodelling after installation of implants using an osteotome technique," *Clinical oral implants research*, vol. 13, no. 6, pp. 595–602, 2002.

[89] L. Martini, M. Fini, G. Giavaresi, and R. Giardino, "Sheep model in orthopedic research: a literature review," *Comparative medicine*, vol. 51, no. 4, pp. 292–299, 2001.